An *h*-adaptive local discontinuous Galerkin method for the Navier–Stokes–Korteweg equations

Lulu Tian [a,b], Yan Xu [c,*], J.G.M. Kuerten [b,d], J.J.W. van der Vegt [b]

[a] *College of Science, China University of Petroleum, Qingdao, Shandong 266580, PR China*
[b] *Mathematics of Computational Science Group, Dept. of Applied Mathematics, University of Twente, P.O. Box 217, 7500 AE Enschede, The Netherlands*
[c] *School of Mathematical Sciences, University of Science and Technology of China, Hefei, Anhui 230026, PR China*
[d] *Computational Multiphase Flow, Dept. of Mechanical Engineering, Eindhoven University of Technology, P.O. Box 513, 5600 MB Eindhoven, The Netherlands*

A B S T R A C T

In this article, we develop a mesh adaptation algorithm for a local discontinuous Galerkin (LDG) discretization of the (non)-isothermal Navier–Stokes–Korteweg (NSK) equations modeling liquid–vapor flows with phase change. This work is a continuation of our previous research, where we proposed LDG discretizations for the (non)-isothermal NSK equations with a time-implicit Runge–Kutta method. To save computing time and to capture the thin interfaces more accurately, we extend the LDG discretization with a mesh adaptation method. Given the current adapted mesh, a criterion for selecting candidate elements for refinement and coarsening is adopted based on the locally largest value of the density gradient. A strategy to refine and coarsen the candidate elements is then provided. We emphasize that the adaptive LDG discretization is relatively simple and does not require additional stabilization. The use of a locally refined mesh in combination with an implicit Runge–Kutta time method is, however, non-trivial, but results in an efficient time integration method for the NSK equations. Computations, including cases with solid wall boundaries, are provided to demonstrate the accuracy, efficiency and capabilities of the adaptive LDG discretizations.

© 2016 Elsevier Inc. All rights reserved.

1. Introduction

In this article, we present a mesh adaptation algorithm for a local discontinuous Galerkin (LDG) method of the (non)-isothermal Navier–Stokes–Korteweg (NSK) equations. The NSK equations, containing the Korteweg expression for the capillary forces together with the Van der Waals equation of state, model the dynamics of compressible flows with liquid–vapor phase transition. This research follows our previous work [22], where we solved the (non)-isothermal NSK equations in conservative form with an LDG method. We emphasize that the proposed LDG discretizations are relatively simple, robust and do not require special regularization terms. Extensive numerical studies in [22] demonstrate the capabilities, accuracy and stability of the LDG discretizations. These numerical examples were performed for the (non)-isothermal NSK equations with periodic boundary conditions and on a uniform mesh.

---

* Corresponding author.
  E-mail addresses: 18661997061@163.com (L. Tian), yxu@ustc.edu.cn (Y. Xu), J.G.M.Kuerten@tue.nl (J.G.M. Kuerten), j.j.w.vandervegt@utwente.nl (J.J.W. van der Vegt).

Solving the NSK equations with phase transition takes large memory and computing time. First, according to the theory of the diffuse interface model [5] and computational examples in [9,15,22], the mesh needs to be sufficiently fine such that several mesh nodes lay inside the width of the interface in order to capture the solution in the interface region accurately. Otherwise, relations for the decay of the energy in case of the isothermal NSK equations and the growth of the entropy in case of the non-isothermal NSK equations will be violated. Second, the third order derivatives of the density, which appear in the NSK equations, require a strict time step limitation in case explicit integration time methods are adopted. When an implicit integration time method is used for the NSK equations, in particular for a large Weber number, a large nonlinear system of ordinary differential equations (ODEs) needs to be solved.

Small mesh sizes are, however, required only in the interface region. Since the LDG method is well suited to deal with hanging nodes, a locally refined mesh can be combined with the LDG discretizations for the (non)-isothermal NSK equations. This will significantly enhance the accuracy and efficiency of the LDG method. In the remaining part of the introduction, we briefly present the non-isothermal NSK equations with solid wall boundary conditions that will be treated in this article. Then we will discuss mesh adaptation.

Consider a fluid in a domain $\Omega \subset \mathbb{R}^d$ with $d = 2$, and let ρ be the density of the fluid, $\mathbf{u}$ the velocity and θ the temperature. The non-isothermal NSK equations, in dimensionless and conservative form, read

$$\frac{\partial \rho}{\partial t} + \nabla \cdot (\rho \mathbf{u}) = 0,$$

$$\frac{\partial \rho \mathbf{u}}{\partial t} + \nabla \cdot (\rho \mathbf{u} \otimes \mathbf{u} + p\mathbf{I}) - \nabla \cdot \tau - \nabla \cdot \xi = \rho \mathbf{g},$$

$$\frac{\partial (\rho E)}{\partial t} + \nabla \cdot ((\rho E + p)\mathbf{u}) - \nabla \cdot ((\tau + \xi) \cdot \mathbf{u}) + \nabla \cdot \mathbf{q} + \nabla \cdot \mathbf{j}_E = \rho \mathbf{g} \cdot \mathbf{u}, \tag{1}$$

in $\Omega \times (0, T]$, with p the pressure, $\mathbf{g}$ the dimensionless acceleration of the gravity and $\otimes$ the tensor product. The viscous stress tensor τ and Korteweg stress tensor ξ are given by

$$\tau = \frac{1}{\mathbb{R}e} \left(\nabla \mathbf{u} + \nabla^T \mathbf{u} - \frac{2}{3} \nabla \cdot \mathbf{u}\mathbf{I} \right),$$

$$\xi = \frac{1}{\mathbb{W}e} \left(\left(\rho \triangle \rho + \frac{1}{2} |\nabla \rho|^2 \right) \mathbf{I} - \nabla \rho \nabla^T \rho \right), \tag{2}$$

with constant Reynolds number $\mathbb{R}e$ and Weber number $\mathbb{W}e$ [15,8]. Here $\mathbf{I}$ is the identity matrix. The Van der Waals equation of state [6,20,15,8,11] is used to represent the pressure in both the liquid and vapor state (characterized by different values of the density ρ), and is given in dimensionless form by

$$p(\theta, \rho) = Rb \frac{\theta \rho}{b - \rho} - a\rho^2 \quad (a, b > 0), \tag{3}$$

where R, a and b are constants. The total energy density is given by

$$\rho E = \rho e + \frac{1}{2} \rho |\mathbf{u}|^2 + \frac{1}{2} \frac{1}{\mathbb{W}e} |\nabla \rho|^2. \tag{4}$$

The specific internal energy e in (4) is given by

$$e = \frac{8}{3} C_v \theta - 3\rho,$$

with C_v the non-dimensional specific heat at constant volume. The heat flux $\mathbf{q}$ and energy flux $\mathbf{j}_E$ through the interface in (1) are defined as

$$\mathbf{q} = -\frac{8C_v}{3\mathbb{W}e\mathbb{P}r} \nabla \theta, \quad \mathbf{j}_E = \frac{1}{\mathbb{W}e} (\rho \nabla \cdot \mathbf{u}) \nabla \rho, \tag{5}$$

with Prandtl number $\mathbb{P}r$.

Initial and boundary conditions have to be set for the non-isothermal NSK equations. The initial conditions are given by

$$\rho(\mathbf{x}, 0) = \rho_0(\mathbf{x}), \ \mathbf{u}(\mathbf{x}, 0) = \mathbf{u}_0(\mathbf{x}), \ \theta(\mathbf{x}, 0) = \theta_0(\mathbf{x}). \tag{6}$$

For the boundary conditions, we consider at a solid surface a contact angle for the density, the no-slip boundary condition for the velocity and a Dirichlet or Neumann boundary condition for the temperature:

$$-\frac{\nabla \rho}{||\nabla \rho||} \cdot \mathbf{n} = \cos(\phi),$$

$$\mathbf{u} = \mathbf{0},$$

$$\theta = \theta_d(\mathbf{x}), \ \text{or} \ \nabla \theta \cdot \mathbf{n} = 0, \tag{7}$$

at $\mathbf{x} \in \partial\Omega, t > 0$. Here ϕ is the contact angle, and $\mathbf{n}$ is the unit outward normal to the boundary. We set the contact angle as $\pi/2$, which means $\nabla\rho \cdot \mathbf{n} = 0$. The boundary condition for the temperature is set as $\nabla\theta \cdot \mathbf{n} = 0$ in the present work.

When the temperature is considered constant, system (1) reduces to the isothermal NSK equations [15,11,4,20,22]. A review of theoretical and numerical methods to solve the (non-)isothermal NSK equations has been presented in our previous work [22]. Due to the Van der Waals equation of state and the nonlinear third order derivative of the mass density, it is a challenge to develop efficient and accurate methods for the (non-)isothermal NSK equations. Recently, important progress has been made to solve the isothermal NSK equations. Examples are: [13] for a finite volume method with second gradient techniques, [11] for a Galerkin method with carefully chosen numerical fluxes, [4] for a finite element method with additional stabilization terms, and [15] for a Galerkin method with functional entropy variables. See also [9] for a discontinuous Galerkin method for the NSK equations in non-conservative form. Very few articles in the literature so far considered numerical methods for the non-isothermal NSK equations. Also, the isothermal NSK equations are frequently solved in a non-conservative form and an additional term is introduced to the total energy, which makes it difficult to extend the numerical discretization to the non-isothermal NSK equations. In contrast, we developed a simple LDG discretization for the isothermal NSK equations in conservative form and extended it in a straightforward way to the non-isothermal case [22]. Recently, Diehl et al. [10] discussed a local discontinuous Galerkin method and mesh adaptation for the isothermal NSK equations in a non-conservative form. In the current article, we focus on mesh adaptation for a LDG method for the non-isothermal NSK equations in conservative form and the effects of solid wall boundaries.

The two commonly used adaptation methods are h-adaptation and p-adaptation [9]. Here h-adaptation refers to the local refinement and coarsening of the computational mesh, and in p-adaptation the polynomial degree can be adjusted in each element. We focus on h-adaptation in the present work. To start the mesh adaptation, we first need a criterion to decide whether an element in the computational mesh needs to be refined or coarsened. The candidate elements for refinement will be refined, and the coarsening of elements depends on their neighbors.

There are two main types of criteria for refinement and coarsening in finite volume and finite element methods: error estimators and heuristic indicators. Error estimators are based on theoretical results, and they are only available when a posteriori error estimates hold. For example, a posteriori error estimates can be found for first order finite volume schemes for scalar conservation laws and nonlinear hyperbolic systems of conservation laws [17,14]. A posteriori error estimates for finite element methods can be found in [1,16,23,24] and for higher order Runge–Kutta discontinuous Galerkin methods for multidimensional nonlinear scalar conservation laws in [7]. Heuristic indicators usually depend on local gradients of thermodynamic variables like density, pressure, energy and entropy. Compared with a posteriori error estimates, heuristic indicators are easy to compute, and are widely used in practical applications [3,25,9,4], but they have a limited theoretical foundation. Several indicators for adaptive Runge–Kutta discontinuous Galerkin methods for hyperbolic conservation laws can be found in [19,27,28]. Since a reliable a posteriori error estimate is currently out of scope for LDG discretizations of the (non-)isothermal NSK equations, a heuristic indicator is chosen in this article, which is based on the density gradient $|\nabla\rho|$.

The outline of this article can be summarized as follows. In Section 2, we briefly discuss an LDG discretization for the (non-)isothermal NSK equations in conservative form and without additional stabilization terms. Boundary conditions are treated in a special way in the LDG discretization. The mesh adaptation method is presented in Section 3. An adaptation criterion is proposed to select candidate elements for refinement and coarsening in the computational mesh. A strategy for refining and coarsening of the candidate elements is then discussed. In Section 4 computational experiments, including simulations with solid wall boundaries, are presented to verify the adaptive LDG method for the (non-)isothermal NSK equations. Finally, we give conclusions and recommendations for future research in Section 5.

2. LDG discretization of the NSK equations

In this section, we will present an LDG method to solve the (non-)isothermal NSK system in $\Omega \subset \mathbb{R}^d$ with $d = 2$. Special attention is given to the solid wall boundary conditions (7). We first introduce some notations used for the description of the LDG discretization.

2.1. Notations

We denote by $\mathcal{T}_h$ a tessellation of Ω with regular shaped elements K, Γ represents all boundary faces of $K \in \mathcal{T}_h$ and $\Gamma_0 = \Gamma \backslash \partial\Omega$. Suppose e is a face shared by the "left" and "right" elements K_L and K_R. The normal vectors $\mathbf{n}_L$ and $\mathbf{n}_R$ on e point, respectively, exterior to K_L and K_R. Let φ be a function on K_L and K_R, which could be discontinuous across e, then the left and right trace are denoted as $\varphi_L = (\varphi|_{K_L})|_e$, $\varphi_R = (\varphi|_{K_R})|_e$, respectively. For more details about these definitions, we refer the reader to [26].

To get the LDG discretization, we define the finite element spaces

$$V_h = \{\phi \in L^2(\Omega) : \phi|_K \in \mathcal{P}^k(K), \forall K \in \mathcal{T}_h\},$$
$$\Sigma_h^d = \{\mathbf{\Phi} = (\phi^{(1)}, \phi^{(2)}, ..., \phi^{(d)})^T \in (L^2(\Omega))^d : \phi^{(i)}|_K \in \mathcal{P}^k(K), \ i = 1, ..., d, \forall K \in \mathcal{T}_h\},$$

with $\mathcal{P}^k(K)$ the space of polynomials of degree up to $k \geq 0$ on $K \in \mathcal{T}_h$. In the present work, the computational mesh is composed of rectangular cells for simplicity, and tensor products of the one-dimensional orthogonal Legendre polynomials are used as basis functions.

The numerical solution is denoted by $\mathbf{U}_h$, where each component of $\mathbf{U}_h$ belongs to the finite element space V_h, and can be written as

$$\mathbf{U}_h(\mathbf{x}, t)|_K = \sum_{l=0}^{N_p} \widehat{\mathbf{U}}_l^K(t) \phi_l^K(\mathbf{x}), \text{ for } \mathbf{x} \in K. \tag{8}$$

Here, $\widehat{\mathbf{U}}_l^K(t)$ are the unknowns in element K and $\phi_l^K(\mathbf{x})$ the basis functions in K.

2.2. LDG discretization of the non-isothermal NSK equations

In this section we will present an LDG discretization for the non-isothermal NSK equations with solid boundaries (7). For details and a similar LDG discretization for the isothermal NSK equations, see [22].

To start with the LDG discretization, we first write the non-isothermal NSK equations (1) as a first-order system and keep the conservative form, given by

$$\rho_t + \nabla \cdot \mathbf{m} = 0,$$
$$\mathbf{m}_t + \nabla \cdot \mathbf{F}(\mathbf{U}) - \nabla \cdot \tau(\mathbf{z}, l) - \nabla \cdot \xi(\rho, \mathbf{r}, g) = \rho \mathbf{g},$$
$$(\rho E)_t + \nabla \cdot \mathbf{G}(\mathbf{U}) - \nabla \cdot ((\tau + \xi) \cdot \mathbf{u}) + \nabla \cdot \mathbf{q} + \nabla \cdot \mathbf{j}_E = \mathbf{g} \cdot \mathbf{m}, \tag{9}$$

and auxiliary equations

$$\mathbf{z} = \nabla \mathbf{u},$$
$$l = \nabla \cdot \mathbf{u},$$
$$\mathbf{r} = \nabla \rho,$$
$$g = \nabla \cdot \mathbf{r},$$
$$\mathbf{q} = -\frac{8 C_v}{3 \mathbb{W}e \mathbb{P}r} \nabla \theta, \tag{10}$$

where

$$\mathbf{u} = \frac{\mathbf{m}}{\rho},$$
$$\tau = \frac{1}{\mathbb{R}e} \left(\mathbf{z} + \mathbf{z}^T - \frac{2}{3} l \mathbf{I} \right),$$
$$\xi = \frac{1}{\mathbb{W}e} \left(\left(\rho g + \frac{1}{2} |\mathbf{r}|^2 \right) \mathbf{I} - \mathbf{r} \mathbf{r}^T \right),$$
$$\theta = \left(\frac{\rho E - \frac{1}{2} \mathbf{m}^2 / \rho - \frac{1}{2 \mathbb{W}e} g^2}{\rho} + 3\rho \right) \frac{3}{8 C_v},$$
$$\mathbf{j}_E = \frac{1}{\mathbb{W}e} \rho l \mathbf{r}, \tag{11}$$

and

$$\mathbf{F}(\mathbf{U}) = \mathbf{m} \otimes \mathbf{u} + p(\rho) \mathbf{I}, \quad \mathbf{G}(\mathbf{U}) = (\rho E + p) \mathbf{u}, \quad \mathbf{U} = \begin{pmatrix} \rho \\ \mathbf{m} \\ \rho E \end{pmatrix}.$$

The LDG discretization for the non-isothermal NSK equations (9)–(10) is now as follows: find $\rho_h, (\rho E)_h, l_h, g_h \in V_h$, and $\mathbf{m}_h, \mathbf{z}_h, \mathbf{r}_h, \mathbf{q}_h \in \Sigma_h^d$, such that for all test functions $\phi, \chi, \varphi, \zeta \in V_h$ and $\psi, \eta, \varsigma, \sigma \in \Sigma_h^d$, the following relations are satisfied

$$\int_K (\rho_h)_t \phi \, dK - \int_K \mathbf{m}_h \cdot \nabla \phi \, dK + \int_{\partial K} \widehat{\mathbf{m}_h} \cdot \mathbf{n} \phi \, ds = 0,$$
$$\int_K (\mathbf{m}_h)_t \psi \, dK - \int_K (\mathbf{F}_h - \tau_h - \xi_h) \cdot \nabla \psi \, dK + \int_{\partial K} (\widehat{\mathbf{F}}_h - \widehat{\tau}_h - \widehat{\xi}_h) \cdot \mathbf{n} \psi \, ds = \int_K \rho_h \mathbf{g} \psi \, dK,$$

$$\int\limits_K ((\rho E)_h)_t \chi \, dK - \int\limits_K (\mathbf{G}_h - (\tau_h + \xi_h) \cdot \mathbf{u}_h + \mathbf{q}_h + (\mathbf{j}_E)_h) \cdot \nabla \chi \, dK +$$

$$\int\limits_{\partial K} (\widehat{\mathbf{G}}_h - (\widehat{\tau}_h + \widehat{\xi}_h) \cdot \widehat{\mathbf{u}}_h + \widehat{\mathbf{q}}_h + \widehat{(\mathbf{j}_E)}_h) \cdot \mathbf{n}\chi \, ds = \int\limits_K \mathbf{g} \cdot \mathbf{m}_h \chi dK, \tag{12}$$

and

$$\int\limits_K \mathbf{z}_h \eta \, dK = -\int\limits_K \mathbf{u}_h \nabla \cdot \eta \, dK + \int\limits_{\partial K} \widehat{\mathbf{u}}_h \eta \cdot \mathbf{n} \, ds,$$

$$\int\limits_K l_h \zeta \, dK = -\int\limits_K \mathbf{u}_h \cdot \nabla \zeta \, dK + \int\limits_{\partial K} \widehat{\mathbf{u}}_h \cdot \mathbf{n}\zeta \, ds,$$

$$\int\limits_K \mathbf{r}_h \varsigma \, dK = -\int\limits_K \rho_h \nabla \cdot \varsigma \, dK + \int\limits_{\partial K} \widehat{\rho}_h \varsigma \cdot \mathbf{n} \, ds,$$

$$\int\limits_K g_h \varphi \, dK = -\int\limits_K \mathbf{r}_h \cdot \nabla \varphi \, dK + \int\limits_{\partial K} \widehat{\mathbf{r}}_h \cdot \mathbf{n}\varphi \, ds,$$

$$\int\limits_K \mathbf{q}_h \sigma dK - \frac{8C_v}{3\mathbb{W}e\mathbb{P}r} \int\limits_K \theta_h \nabla \cdot \sigma \, dK + \frac{8C_v}{3\mathbb{W}e\mathbb{P}r} \int\limits_{\partial K} \widehat{\theta}_h \sigma \cdot \mathbf{n} \, ds = 0, \tag{13}$$

where

$$\widehat{\mathbf{u}}_h = \frac{\widehat{\mathbf{m}}_h}{\widehat{\rho}_h},$$

$$\widehat{\tau}_h = \frac{1}{\mathbb{R}e} \left(\widehat{\mathbf{z}}_h + \widehat{\mathbf{z}}_h^T - \frac{2}{3}\widehat{l}_h\mathbf{I} \right),$$

$$\widehat{\xi}_h = \frac{1}{\mathbb{W}e} \left(\left(\widehat{\rho}_h\widehat{g}_h + \frac{1}{2}|\widehat{\mathbf{r}}_h|^2 \right) I - \widehat{\mathbf{r}}_h\widehat{\mathbf{r}}_h^T \right),$$

$$\theta_h = \left(\frac{(\rho E)_h - \frac{1}{2}\mathbf{m}_h^2/\rho_h - \frac{1}{2\mathbb{W}e}g_h^2}{\rho_h} + 3\rho_h \right) \frac{3}{8C_v},$$

$$\widehat{(\mathbf{j}_E)}_h = \frac{1}{\mathbb{W}e} \widehat{\rho}_h\widehat{l}_h\widehat{\mathbf{r}}_h, \tag{14}$$

and

$$\mathbf{F}_h = \mathbf{F}(\mathbf{U}_h), \quad \mathbf{G}_h = \mathbf{G}(\mathbf{U}_h), \quad \mathbf{U}_h = \begin{pmatrix} \rho_h \\ \mathbf{m}_h \\ (\rho E)_h \end{pmatrix}.$$

The terms denoted with a hat in (12), (13) and (14) are single valued functions on each edge of element K, and are called numerical fluxes. We discuss the choices of the numerical fluxes in the next section.

2.3. Numerical fluxes

For the numerical fluxes in the LDG discretizations, solid wall boundaries (7) should be accounted for. Consider an edge $e \in \partial K$.

- If e is an interior edge, we choose the Lax–Friedrichs flux for the convective part and central numerical fluxes for the other flux terms. This means

$$\widehat{\mathcal{F}_h}|_e = \frac{1}{2}(\mathcal{F}_h|_L + \mathcal{F}_h|_R - \alpha(\mathbf{U}_h|_R - \mathbf{U}_h|_L)), \quad \text{with } \mathcal{F}_h = \begin{pmatrix} \mathbf{m}_h \\ \mathbf{F}_h \\ \mathbf{G}_h \end{pmatrix},$$

$$\widehat{\mathbf{m}}_h|_e = \frac{1}{2}(\mathbf{m}_h|_L + \mathbf{m}_h|_R), \quad \widehat{\rho}_h|_e = \frac{1}{2}(\rho_h|_L + \rho_h|_R),$$

$$\widehat{\mathbf{r}}_h|_e = \frac{1}{2}(\mathbf{r}_h|_L + \mathbf{r}_h|_R), \quad \widehat{\mathbf{z}}_h|_e = \frac{1}{2}(\mathbf{z}_h|_L + \mathbf{z}_h|_R),$$

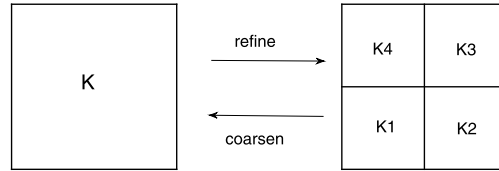**Fig. 1.** Refinement of quadrilaterals.

$$\widehat{l_h}|_e = \frac{1}{2}(l_h|_L + l_h|_R), \quad \widehat{g_h}|_e = \frac{1}{2}(g_h|_L + g_h|_R),$$

$$\widehat{\theta_h}|_e = \frac{1}{2}(\theta_h|_L + \theta_h|_R), \quad \widehat{\mathbf{q}_h}|_e = \frac{1}{2}(\mathbf{q}_h|_L + \mathbf{q}_h|_R), \tag{15}$$

with α the global maximum of the absolute eigenvalue of $\frac{\partial \mathcal{F}_h}{\partial \mathbf{U}_h}$ [22].

- If e is an edge at the solid wall boundary of the domain, the numerical fluxes for the density, momentum and temperature on e are given by

$$\mathbf{n} \cdot \widehat{(\nabla \rho)_h}|_e = 0, \; \widehat{\mathbf{m}_h}|_e = \mathbf{0}, \; \mathbf{n} \cdot \widehat{(\nabla \theta)_h}|_e = 0, \tag{16}$$

and the numerical fluxes for the remaining terms use data from the interior of the domain. In the LDG discretization, we have introduced extra variables $\mathbf{r} = \nabla \rho, \mathbf{q} = \nabla \theta$ to rewrite the original system as a first order system. We set the boundary conditions for ρ and θ as values taken from the inside of the domain and $\mathbf{n} \cdot \widehat{\mathbf{r}} = 0, \mathbf{n} \cdot \widehat{\mathbf{q}} = 0$.

3. Mesh adaptation

In this section mesh adaptation for two-dimensional phase transition problems will be considered. We will first discuss refinement and coarsening of quadrilaterals, then present a criterion to select candidate elements in the computational mesh for refinement and coarsening, and finally we will discuss the mesh adaptation procedure. A flow chart of the mesh adaptation algorithm will be given at the end of this section.

3.1. Refinement and coarsening of quadrilaterals

In this section we will discuss the refinement of a single quadrilateral and the coarsening of children quadrilaterals. We assume that

- a background mesh with rectangular elements is used in the computational mesh,
- an element (called parent element) is always divided into 4 child elements with equal size,
- 4 child elements obtained from the same parent element can be coarsened to the parent element.

A description of the refinement of a parent quadrilateral and the coarsening of the child quadrilaterals is shown in Fig. 1. During mesh adaptation, the L^2-projection is used to compute the LDG coefficients, $\widehat{\mathbf{U}}_l^K$ in (8). For example in Fig. 1, L^2-projection in the refinement process means that the degrees of freedom on sub-element Ki are obtained by L^2-projection from the parent element K onto element Ki for $i = 1, \cdots, 4$,

$$\int_{Ki} \mathbf{U}_h^{Ki}(\mathbf{x})\phi_l^{Ki}(\mathbf{x})d\mathbf{x} = \int_{Ki} \mathbf{U}_h^K(\mathbf{x})\phi_l^{Ki}(\mathbf{x})d\mathbf{x}, \quad l = 0, \cdots, N_p - 1.$$

Here ϕ_l^{Ki} is the l-th basis function on element Ki. L^2-projection in the coarsening step requires that the degrees of freedom on the parent element K are obtained by L^2-projection from sub-elements Ki onto element K,

$$\int_K \mathbf{U}_h^K(\mathbf{x})\phi_l^K(\mathbf{x})d\mathbf{x} = \sum_{i=1}^4 \int_{Ki} \mathbf{U}_h^{Ki}(\mathbf{x})\phi_l^K|_{Ki}(\mathbf{x})d\mathbf{x}, \quad l = 0, \cdots, N_p - 1,$$

where $\phi_l^K|_{Ki}$ is the basis function ϕ_l^K restricted to the child element Ki. For detailed procedures for refinement of quadrilaterals and the required L^2-projection, see [9,28].

3.2. Candidate elements for refinement and coarsening

In this section, we will provide a criterion to select candidate elements in the computational mesh for refinement and coarsening based on the locally largest value of the density gradient. Since the density changes rapidly at the interfacial
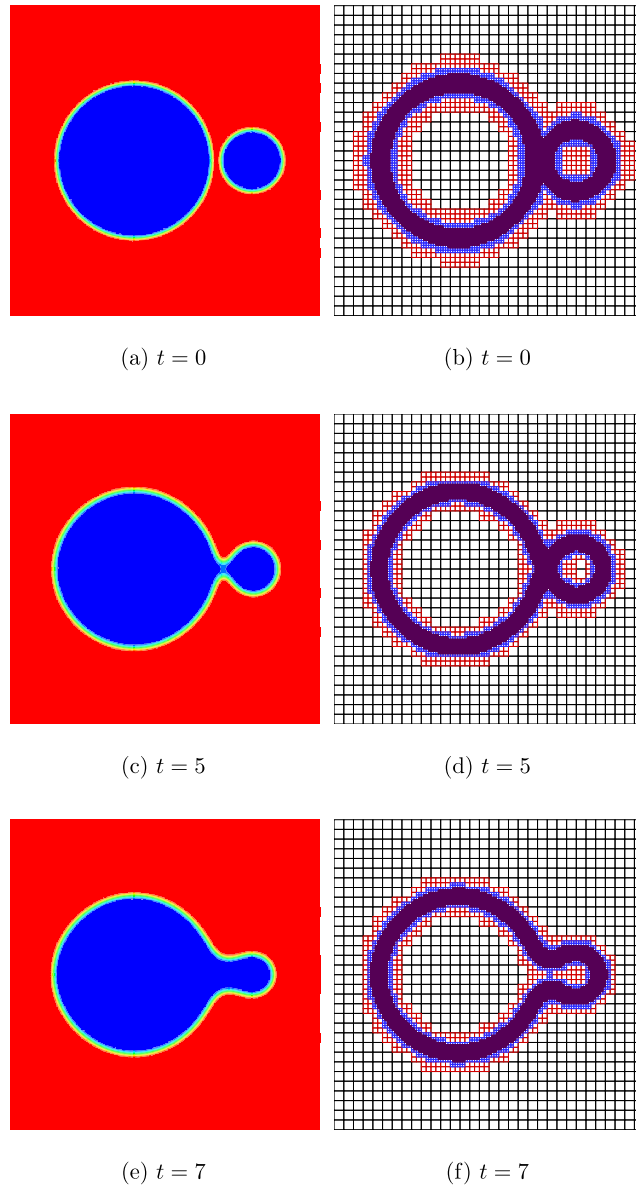
(a) $t = 0$ (b) $t = 0$

(c) $t = 5$ (d) $t = 5$

(e) $t = 7$ (f) $t = 7$

Fig. 2. Example 4.1: time sequence of the coalescence of vapor bubbles and the adapted mesh. Isothermal NSK equations with $\mathbb{R}e = 512$, $\mathbb{W}e = 65\,500$ and pressure formulation (19) at $\theta = 0.85$. Initial conditions (20) and periodic boundaries. Initially uniform mesh of 32×32 elements with three levels of refinement, $\eta_{upp} = 0.05$, $\eta_{low} = 0.01$ in adaptation criterion (18). Left: density profile, Right: corresponding computational mesh.

region, the elements near the interface need to be refined. As the topology of the flow field changes, elements which were refined from a parent element and are not close to the interface anymore, need to be coarsened.

In this adaptation criterion, an indicator η_ρ^K for each element K is defined based on the gradients of the density on element K, and its direct and indirect neighbors [9],

$$\eta_\rho^K = \max\{\frac{\text{diam}(K^j)}{|K^j|}||\nabla\rho||_{L^2(K^j)}|K^j \text{ is neighbor of } K \text{ of degree at most } m\}. \tag{17}$$

Here $\text{diam}(K^j)$ and $|K^j|$ represent the longest edge and the area of element K^j, respectively. The element K^j is a neighbor of element K of degree at most m if there exist $m + 1$ cells in the computational mesh with

$$K = K^0,$$

$$K^l \text{ is a neighbor of } K^{l+1}, \quad l = 0, 1, \cdots, m.$$

Algorithm 1 Refinement of candidate elements.

call candidate elements for refinement by criterion (18) $Cells_{refine}$
for each element K in $Cells_{refine}$ **do**
   for each neighbor $\widetilde{K}$ of K **do**
      if $\widetilde{K}$ is not in $Cells_{refine}$ and the refinement level of $\widetilde{K} <$ the
      refinement level of K **then**
         add $\widetilde{K}$ to $Cells_{refine}$, this $\widetilde{K}$ will become a new K in $Cells_{refine}$
      end if
   end for
end for

Algorithm 2 Coarsening of candidate elements.

call candidate elements for coarsening by criterion (18) $Cells_{coarse}$
for each element K in $Cells_{coarse}$ **do**
   set K_p as the parent cell of K
   if all the children of K_p are in $Cells_{coarse}$ **then**
      if the refinement level of all the neighbors of $\widetilde{K}_p <$ the
      refinement level of K **then**
         keep K in $Cells_{coarse}$
      else
         delete K from $Cells_{coarse}$
      end if
   else
      delete K from $Cells_{coarse}$
   end if
end for

Here $m = 0$ means only a contribution of element K and $m = 1$ contributions of K and its direct neighbors. Note that the computation of η_ρ^K for all cells is expensive for large m, but for $m = 0$ it leads to unstable results or slows down the iterative linear solvers [9]. We choose $m = 1$ throughout the present work.

Based on the indicators for the elements in the computational mesh, we select candidate elements for refinement and coarsening. We define the refinement level of the initial coarse elements by 0. An initial coarse element can be refined at most LEV times. For each element K in the computational mesh,

$$\text{if } \eta_\rho^K > \eta_{upp} \text{ and the refinement level of } K < LEV$$

we mark K as a candidate element for refinement,

$$\text{else if } \eta_\rho^K < \eta_{low} \text{ and the refinement level of } K > 0$$

then we mark K as a candidate element for coarsening, $\qquad\qquad\qquad\qquad\qquad$ (18)

with problem dependent parameters η_{upp}, η_{low} and

$$\eta_{upp} > \eta_{low} > 0.$$

3.3. Strategy for refinement and coarsening

In this section we will present a refinement and coarsening algorithm for the LDG discretization, given candidate elements selected through the adaptation criterion (18). Although the LDG method allows locally many refinement levels, we impose that the difference in refinement levels between two neighboring elements is less than two to improve the stability and accuracy of the LDG method.

To guarantee the difference in refinement levels between two neighboring elements less than two, we use the "refinement must, coarsening can" strategy in the mesh adaptation. This strategy means that a candidate refinement cell is definitely refined and coarsening of a candidate element K depends on the neighbors of element K.

Algorithm 1 and 2 result in lists for refinement and coarsening, respectively. In Algorithm 1, all candidate refinement elements will be refined, and some neighbors of these elements are added to the refinement list to ensure mesh quality. In Algorithm 2, a candidate coarsening element K may not be coarsened due to the refinement level difference with the neighbors.

3.4. Flow chart for mesh adaptation

Next, we provide a flow chart to illustrate the adaptive LDG method. Given the maximum refinement level LEV and the final time T,
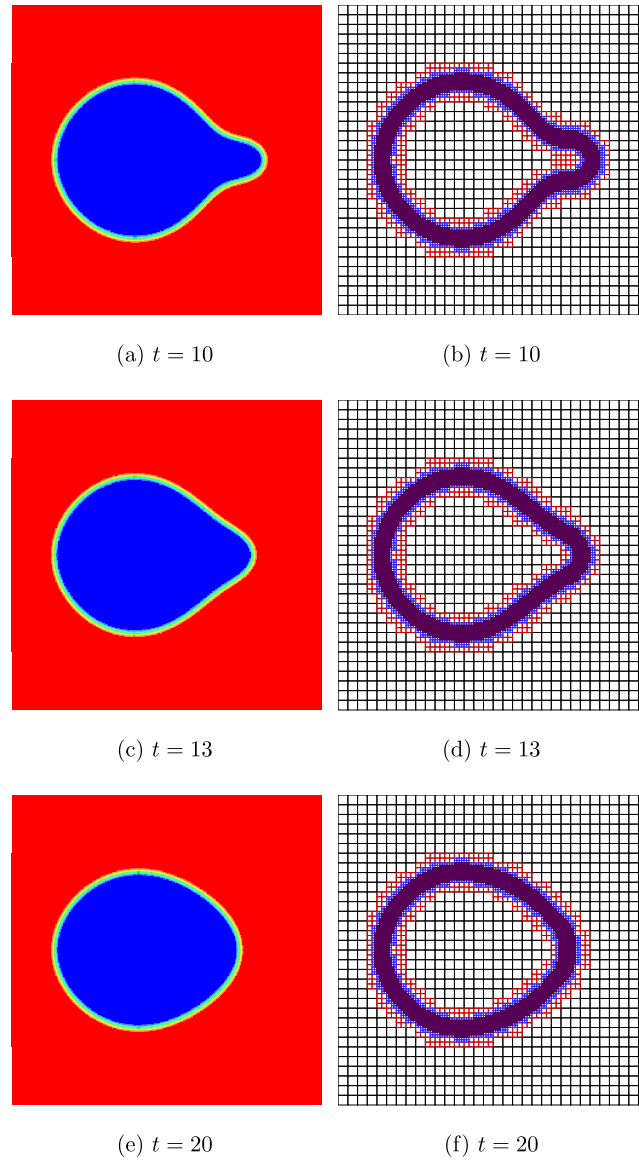
Fig. 3. Example 4.1: time sequence of the coalescence of vapor bubbles and the adapted mesh. Isothermal NSK equations with $\mathbb{R}e = 512$, $\mathbb{W}e = 65\,500$ and pressure formulation (19) at $\theta = 0.85$. Initial conditions (20) and periodic boundaries. Initially uniform mesh of 32×32 elements with three levels of refinement, $\eta_{upp} = 0.05$, $\eta_{low} = 0.01$ in adaptation criterion (18). Left: density profile, Right: corresponding computational mesh.

- Step 1. Partition the domain into uniform rectangles, compute the degrees of freedom on each element K by projecting the initial solution on element K, and set the level of element K to be 0. An initial computational mesh $\mathcal{T}_h(t_0)$, the level of the elements in $\mathcal{T}_h(0)$ and the degrees of freedom $\{\widehat{\mathbf{U}}^K(0), K \in \mathcal{T}_h(0)\}$ are obtained.
- Step 2. Given a computational mesh $\mathcal{T}_h(t_n)$ at time $t = t_n$, the refinement level of the elements in the mesh $\mathcal{T}_h(t_n)$ and the degrees of freedom $\{\widehat{\mathbf{U}}^K(t_n), K \in \mathcal{T}_h(t_n)\}$
  - detect candidate elements for refinement and coarsening in the computational mesh through adaptation criterion (18),
  - create lists of elements for refinement and coarsening with Algorithm 1 and 2, respectively,
  - for each element K in the refinement list, divide element K into four uniform child elements Ki, $i = 1, 2, 3, 4$, increase the refinement level of elements Ki by one, and get the degrees of freedom on elements Ki from element K by L^2 projection,
  - when four cells in the coarsening list are all children of the same parent element K_p, merge them and get the degrees of freedom on K_p from its children elements by L^2 projection.

  A new adapted mesh $\mathcal{T}_h(t_{n+1})$ and the refinement level of the elements in $\mathcal{T}_h(t_{n+1})$ are obtained.

(a) mass loss   (b) energy decrease
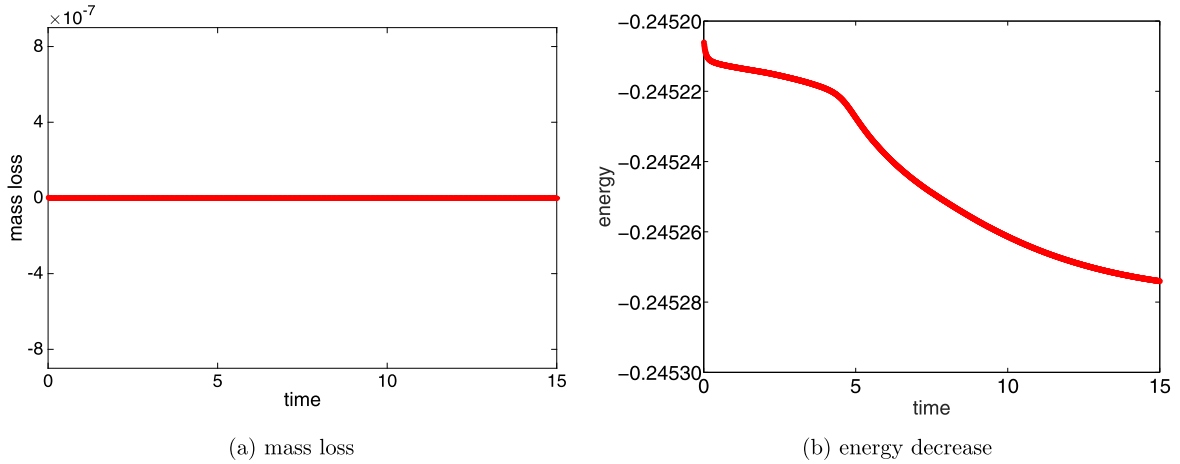
Fig. 4. Example 4.1: evolution of mass and energy during the coalescence of vapor bubbles on an adapted mesh. Isothermal NSK equations with $\mathbb{R}e = 512$, $\mathbb{W}e = 65\,500$ and pressure formulation (19) at $\theta = 0.85$. Initial conditions (20) and periodic boundaries. Initially uniform mesh of 32×32 elements with three levels of refinement, $\eta_{upp} = 0.05$, $\eta_{low} = 0.01$ in adaptation criterion (18).

(a) mass loss   (b) energy
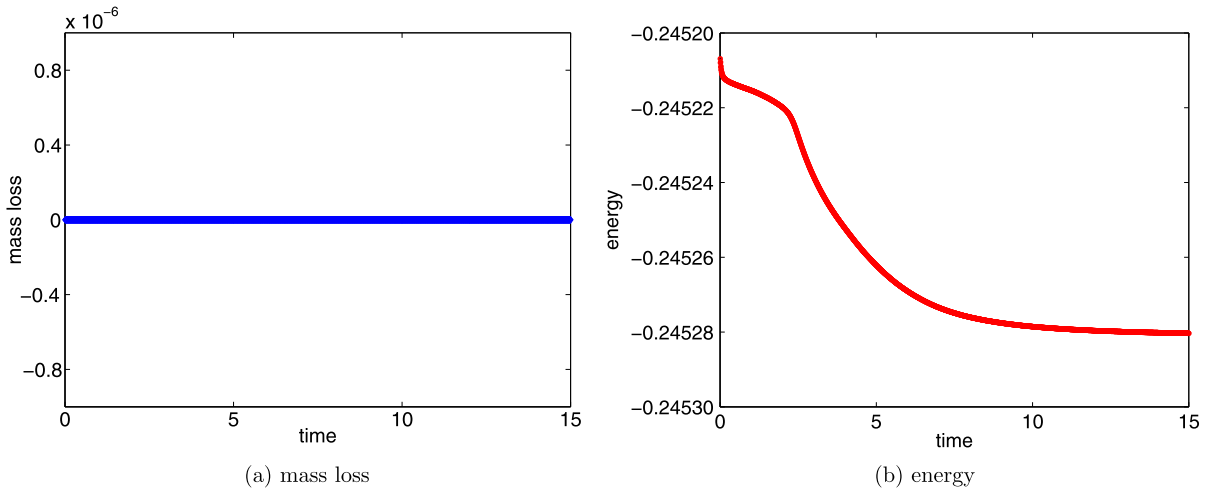
Fig. 5. Example 4.1: evolution of mass loss and energy during the coalescence of vapor bubbles on a uniform mesh of 256×256 elements. Isothermal NSK equations with $\mathbb{R}e = 512$, $\mathbb{W}e = 65\,500$ and pressure formulation (19) at $\theta = 0.85$. Initial conditions (20) and periodic boundaries.

- Step 3. Evolve the solution from t_n to t_{n+1} with the LDG method: i.e. solve a system of ODEs resulting from the LDG discretizations through an implicit RK time method, and obtain $\{\widehat{\mathbf{U}}^K(t_{n+1}), K \in \mathcal{T}_h(t_{n+1})\}$.
- Step 4. If $t_{n+1} < T$, go to Step 2.

Note that the initial coarse mesh is uniform, we perform Step 2 therefore LEV times to capture the initial interface accurately. The degrees of freedom on the refined elements in the initial mesh are obtained by L^2 projection from the initial solution. Since it is not necessary to change the adapted mesh every time step during a simulation for the (non-)isothermal NSK equations, we apply Step 2 every 10 time steps in the numerical simulations discussed in the next section.

4. Numerical examples

In this section, numerical simulations will be presented to demonstrate the adaptive LDG discretizations for the (non-)isothermal NSK equations. First, we will consider simulations of the coalescence of vapor bubbles in a liquid. In our previous work we performed these simulations on a uniform mesh [22]. The same examples are computed here on an adaptive mesh, and the results will be compared with those on a uniform mesh. Second, we will discuss the structure of the Jacobi matrix for an adapted mesh for the non-isothermal NSK equations. Finally, we will study the shape of a vapor bubble and a liquid droplet in a domain with solid wall boundaries and prescribed contact angles, which are challenging problems

Table 1

Adaptive mesh for the simulations of the examples. (a) N_0: initial number of elements; (b) TDT: total times of refinement and coarsening; (c) N_T: number of elements at the final time; (d) $\bar{N}$: average number of elements, defined by $\bar{N} = (\sum_{q=0}^{TOT} N_q)/TOT$ where N_q is the number of elements at the q-th time level and TOT is the total number of time levels; and (e) PR: the percentage ratio of $\bar{N}$ to the number of elements if a uniform mesh would be used, i.e. $PR = 100\bar{N}/M^2$ with M the number of elements in one direction in a uniform mesh. The uniform mesh has the same resolution in the interfacial region as the adapted mesh.

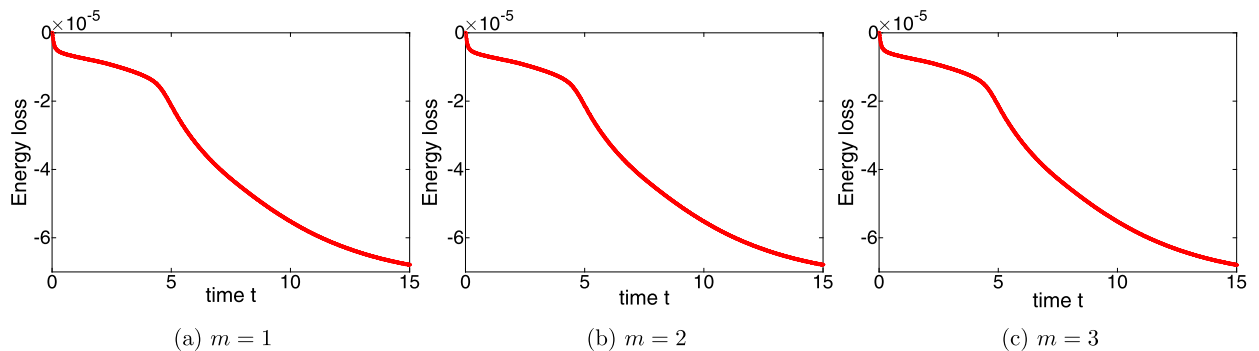| Case	N_0	TDT	N_T	$\bar{N}$	PR
Example 4.1	9736	196	7570	8250	12.60
Example 4.3	4297	154	3097	3851	9.63
Example 4.4	2467	30	2488	2484	6.21

Fig. 6. Example 4.1: evolution of energy loss during the coalescence of vapor bubbles on an adapted mesh with various values for number m defined in Section 3.2. Three levels of refinement. Isothermal NSK equations with $\mathbb{R}e = 512$, $\mathbb{W}e = 65\,500$.
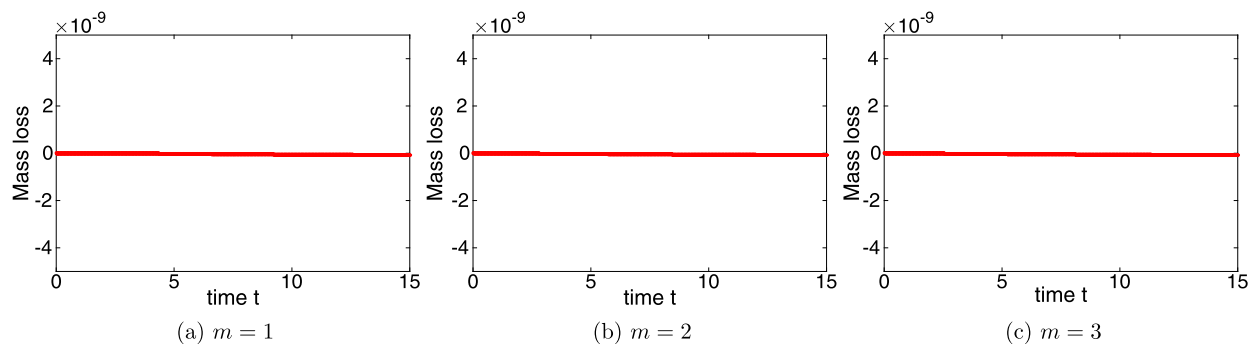

Fig. 7. Example 4.1: evolution of mass loss during the coalescence of vapor bubbles on an adapted mesh with various values for number m defined in section 3.2. Three levels of refinement. Isothermal NSK equations with $\mathbb{R}e = 512$, $\mathbb{W}e = 65\,500$.

in fluid mechanics. One example, representing a vapor bubble in contact with a solid wall, was studied in [13] by a finite difference scheme and an explicit time integration method on a uniform mesh. The last example describes a liquid droplet on a solid surface, which was recently studied in [15] by a semi-discrete Galerkin method and a special time integration method on a uniform mesh.

We use a relatively simple LDG method to solve the (non)-isothermal NSK equations in conservative form on the adapted mesh. The adapted mesh is obtained using adaptation criterion (18), Algorithm 1 and Algorithm 2 in Section 3. Note that for the selection criterion given by (18), $m = 1$ is chosen in (17) to compute the indicator η_ρ^K for each element K. This means only contributions of element K and its direct neighbors are used, which saves many computations compared to [9], where $m = 4, 8$ was chosen. The computational domain in all simulations is $[0, 1]^2$, linear basis functions are used in all numerical examples.

Due to the third derivative of the density in the NSK equations, a diagonally implicit Runge–Kutta (DIRK) time integration method [2] is adopted to solve the ODEs resulting from the LDG discretizations. In particular, a second order DIRK scheme is used for all the numerical examples discussed in this section.
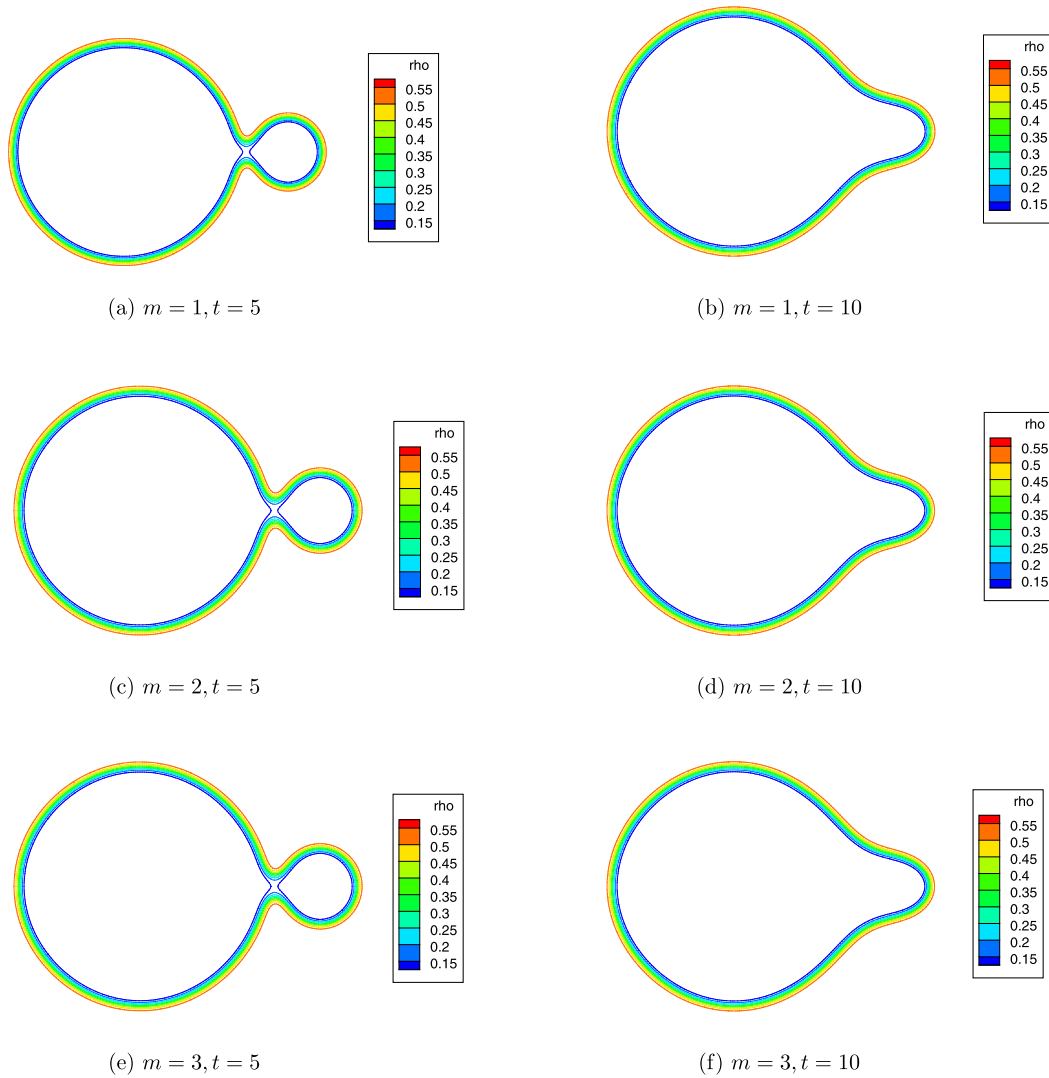
(a) $m = 1, t = 5$

(b) $m = 1, t = 10$

(c) $m = 2, t = 5$

(d) $m = 2, t = 10$

(e) $m = 3, t = 5$

(f) $m = 3, t = 10$

Fig. 8. Example 4.1: Coalescence of vapor bubbles on an adapted mesh with various values for *m*, three levels of refinement. The interface is represented by the sharp gradient in the density; data on the third (finest) mesh level are used. Isothermal NSK equations with $\mathbb{R}e = 512$, $\mathbb{W}e = 65\,500$.

4.1. Coalescence of vapor bubbles in a liquid

An important test case is a simulation of the coalescence of two vapor bubbles in a liquid. We simulate the coalescence of vapor bubbles in a liquid for both the isothermal and non-isothermal NSK equations on adapted meshes.

Example 4.1 *(Coalescence of vapor bubbles in a liquid, isothermal case).*

This example was also studied with a Galerkin method on a uniform mesh [15], and with a finite element method including additional stabilization terms on an adaptive mesh [4]. In this example, the Van der Waals equation of state (3) is chosen for the isothermal NSK equations as [4,15,22]

$$p(\rho) = \frac{8\theta\rho}{27(1 - \rho)} - \rho^2, \tag{19}$$

with a dimensionless temperature $\theta = 0.85$. The parameters of the isothermal NSK equations are set as $\mathbb{R}e = 512$, $\mathbb{W}e = 65\,500$.

The initial conditions are

$$\rho_0(\mathbf{x}) = \rho_1 + \frac{1}{2}(\rho_2 - \rho_1)\sum_{i=1}^{2}\tanh\left(\frac{(d_i(\mathbf{x}) - r_i)}{2}\sqrt{\mathbb{W}e}\right), \quad \mathbf{u} \equiv \mathbf{0}, \tag{20}$$
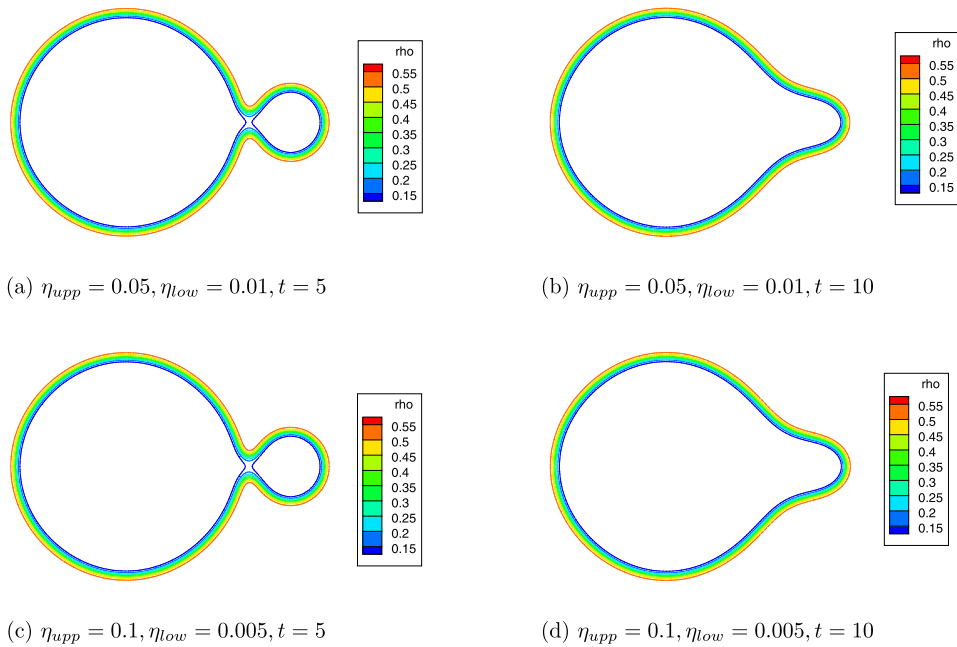
(a) $\eta_{upp} = 0.05, \eta_{low} = 0.01, t = 5$

(b) $\eta_{upp} = 0.05, \eta_{low} = 0.01, t = 10$

(c) $\eta_{upp} = 0.1, \eta_{low} = 0.005, t = 5$

(d) $\eta_{upp} = 0.1, \eta_{low} = 0.005, t = 10$

Fig. 9. Example 4.1: Coalescence of vapor bubbles on an adapted mesh, three levels of refinement with $m = 2$ and various values of η_{upp}, η_{low}. The interface is represented by the sharp gradient in the density; data on the third (finest) mesh level are used. Isothermal NSK equations with $\mathbb{R}e = 512$, $\mathbb{W}e = 65\,500$.

with $\rho_1 = 0.1$, $\rho_2 = 0.6$. Here $d_i(\mathbf{x}) = ||\mathbf{x} - \mathbf{x}_i||$ is the Euclidean distance and the points $\mathbf{x}_i$ are equal to $\mathbf{x}_1 = (0.4, 0.5)$ and $\mathbf{x}_2 = (0.78, 0.5)$, respectively. The radii of the two bubbles are $r_1 = 0.25$ and $r_2 = 0.1$. Similar to [22], periodic boundary conditions are used for all variables.

The initial coarse mesh is set at 32×32 elements with three levels of refinement in the interface region. Then the adapted mesh has the same resolution in the interfacial region as for the computations on the uniform mesh in [22]. The parameters in (18) are chosen as $\eta_{upp} = 0.05$, $\eta_{low} = 0.01$.

The results of the adaptive LDG method for Example 4.1 are shown in Figs. 2–4. Figs. 2–3 describe the coalescence of bubbles, showing that the bubbles merge into one vapor bubble by capillarity and pressure forces. Fig. 4 shows the evolution of mass and energy during the simulation on the adapted mesh, indicating that the mass is conserved and the energy is decreasing in time. It is noticeable that the results for the mass loss and energy decrease on the adapted mesh are very similar to the results in Fig. 5 for the uniform mesh used in [22].

The numbers of elements in the adapted mesh at the initial, average and final time are shown in Table 1. These numbers are much less than 256^2, the number of elements in the uniform mesh used in [22]. Compared with the uniform mesh with equivalent mesh resolution in the interface region, the adaptive LDG method leads to a considerably smaller nonlinear system of algebraic equations that is solved by the Newton-GMRES method. Note that the computing time for the simulation of the coalescence of bubbles on the adaptive mesh reduces to about 1/3 of the simulation time on a uniform mesh.

In the following, results of several tests are presented to verify the efficiency of different refinement/coarsening strategies concerning the degree of neighbor m defined in Section 3.2 and indicator thresholds η_{upp}, η_{low} used in Algorithms 1 and 2.

1. The results of mesh adaptation with various values of m for the same numerical example are very similar, see Figs. 6–8. The only difference is that simulations with a larger value of m result in slightly more elements in the computational mesh. In Example 4.1, when $m = 1$, the maximum number of elements in the computational mesh is 9669 and the average number of elements in the computational mesh is 7508; when $m = 2$, the maximum number of elements is 10943, and the average number of elements is 8463; when $m = 3$, the maximum number of elements is 11309, and the average number of elements is 8738.

2. Regarding the indicator thresholds η_{upp}, η_{low}, the difference resulting from various values of η is very small. The computed bubble interfaces (shown as the strong gradient in density) are almost the same, as can be seen from Figs. 8 and 9. The number of elements used in the computational mesh for larger η_{upp} and smaller η_{low} is very similar. In Example 4.1, when $m = 2$, for $\eta_{upp} = 0.05$, $\eta_{low} = 0.01$, the maximum number of elements in the computational mesh is 10943, the average number of elements in the computational mesh is 8463; while for $\eta_{upp} = 0.1$, $\eta_{low} = 0.005$, the maximum number of elements in the computational mesh is 10271, the average number of elements in the computational mesh is 7959.

3. The different adaptation strategies discussed in the previous section gave only minor differences, also in comparison with the results on a uniformly refined mesh, as we presented in [22]. This demonstrates that the interface is well resolved, as can also be seen from the figures with the adapted mesh results.
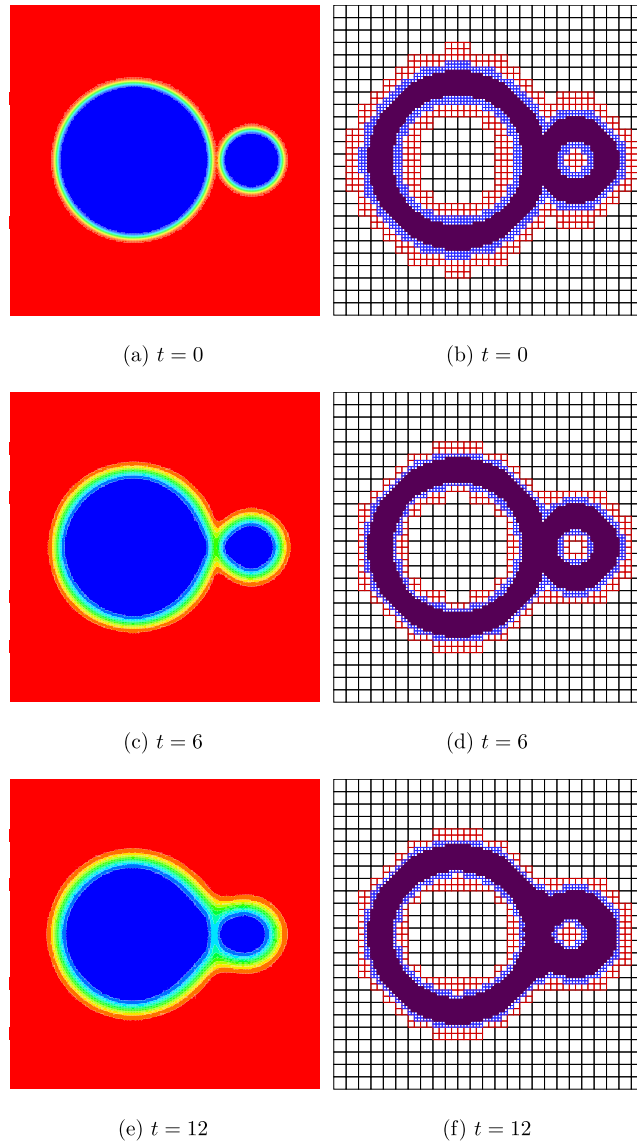
(a) $t = 0$ (b) $t = 0$

(c) $t = 6$ (d) $t = 6$

(e) $t = 12$ (f) $t = 12$

Fig. 10. Example 4.2: time sequence of the coalescence of bubbles and the adapted mesh. Non-isothermal NSK equations with $\mathbb{R}e = 950$, $\mathbb{W}e = 34\,455$ and pressure formulation (21). Initial condition (22) and periodic boundary conditions. Initially uniform mesh of 25×25 elements with three levels of refinement, $\eta_{upp} = 0.05$, $\eta_{low} = 0.01$ in adaptation criterion (18). Left: density profile, Right: corresponding computational mesh.

Example 4.2 *(Coalescence of vapor bubbles in a liquid, non-isothermal case).*

In this example we compute the coalescence of vapor bubbles in a liquid for the non-isothermal NSK equations. The parameters of the non-isothermal NSK equations are set as $\mathbb{R}e = 950$, $\mathbb{W}e = 34\,455$ and $\mathbb{P}r = 0.843$. The Van der Waals equation of state (3) is chosen as in [22,8,18]

$$p(\rho) = \frac{8\theta\rho}{(3 - \rho)} - 3\rho^2. \tag{21}$$

The initial conditions are

$$\rho_0(\mathbf{x}) = \rho_1 + \frac{1}{2}(\rho_2 - \rho_1) \sum_{i=1}^{2} \tanh\left(\frac{(d_i(\mathbf{x}) - r_i)}{2}\sqrt{\mathbb{W}e} \right),$$

$$\mathbf{u} \equiv \mathbf{0}, \quad \theta(\mathbf{x}) = 0.989, \tag{22}$$

with $\rho_1 = 0.795$, $\rho_2 = 1.213$. Here $d_i(\mathbf{x}) = ||\mathbf{x} - \mathbf{x}_i||$ is the Euclidean distance and the points $\mathbf{x}_i$ are equal to $\mathbf{x}_1 = (0.4, 0.5)$ and $\mathbf{x}_2 = (0.78, 0.5)$, respectively. The radii of the two bubbles are $r_1 = 0.25$ and $r_2 = 0.1$.
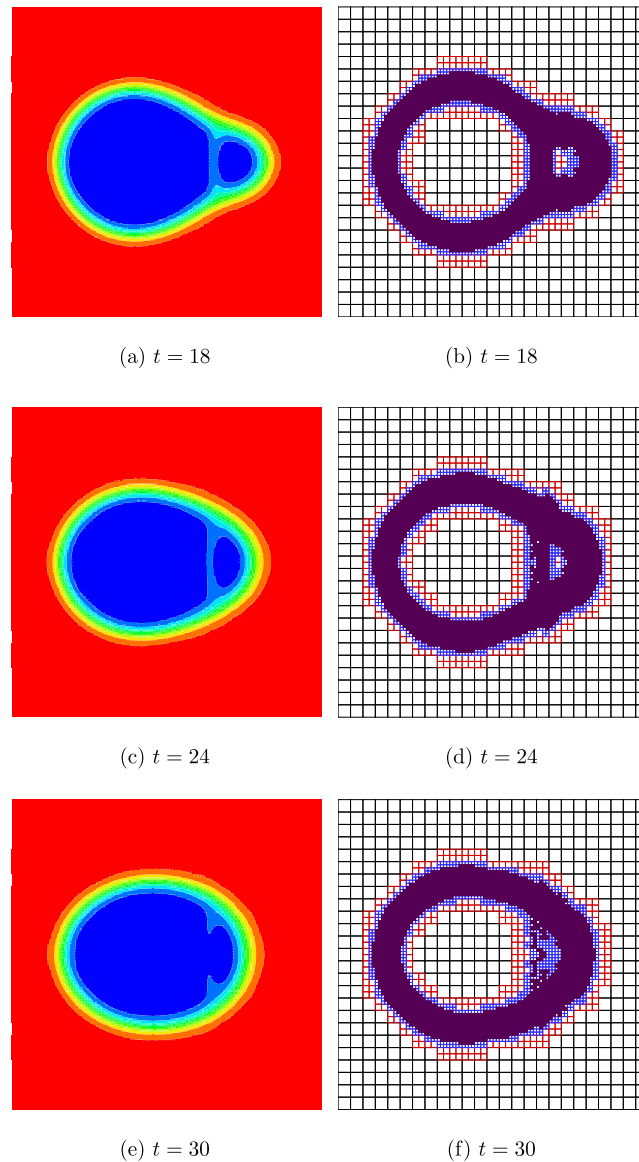
(a) $t = 18$ (b) $t = 18$

(c) $t = 24$ (d) $t = 24$

(e) $t = 30$ (f) $t = 30$

Fig. 11. Example 4.2: time sequence of the coalescence of bubbles and the adapted mesh. Non-isothermal NSK equations with $\mathbb{R}e = 950$, $\mathbb{W}e = 34\,455$ and pressure formulation (21). Initial condition (22) and periodic boundary conditions. Initially uniform mesh of 25×25 elements with three levels of refinement, $\eta_{upp} = 0.05$, $\eta_{low} = 0.01$ in adaptation criterion (18). Left: density profile, Right: corresponding computational mesh.

The initial uniform mesh is set at 25×25 elements with three levels of refinement in the interface region. The parameters in adaptation criterion (18) are chosen as $\eta_{upp} = 0.05$, $\eta_{low} = 0.01$. The adapted mesh then has the same resolution in the interfacial region as the uniform mesh used in [22].

The results of the adaptive LDG method for Example 4.2 are shown in Figs. 10–11. Similar to the results for the isothermal case in Example 4.1, Figs. 10–11 describe the process of the coalescence of the vapor bubbles, showing that the bubbles merge into one vapor bubble by capillarity and pressure forces. Fig. 12 shows the evolution of mass, entropy, momentum along one direction and energy, indicating that the numerical mass, momentum and energy are conserved and the entropy is generally increasing in time.

4.2. DIRK time integration method for an adapted mesh

In this section we will consider a diagonally implicit Runge–Kutta time method on an adapted mesh. In particular, we will present the Jacobi matrix for an example of the non-isothermal NSK equations in a uniform and an adapted mesh, respectively. For the implementation of the DIRK method and the computation of the Jacobi matrix, see [22].
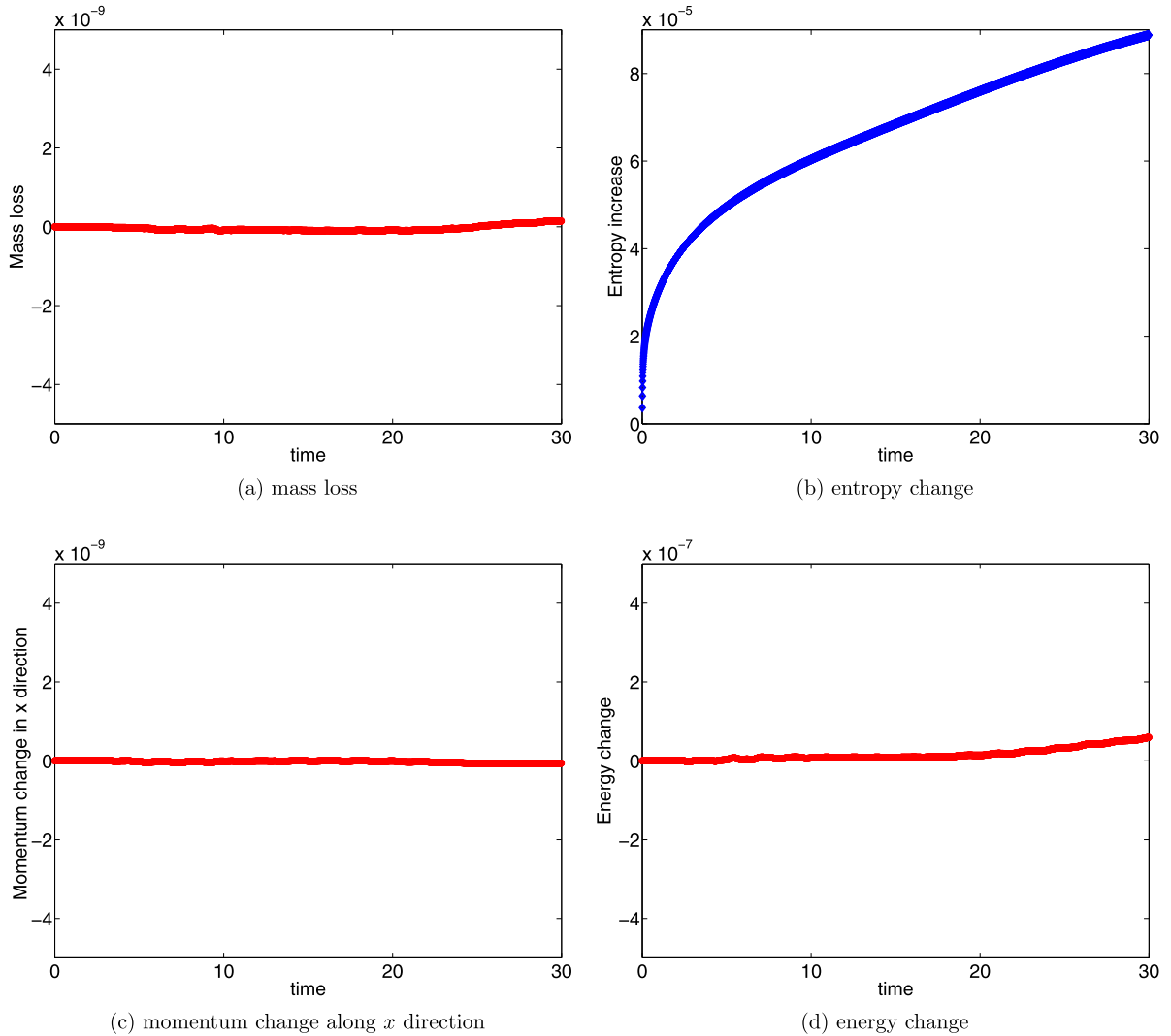
Fig. 12. Example 4.2: evolution of changes in numerical mass, entropy, momentum and energy during the coalescence of vapor bubbles. Non-isothermal NSK equations with $\mathbb{R}e = 950$, $\mathbb{W}e = 34\,455$ and pressure formulation (21). Initial condition (22) and periodic boundary conditions. Initially uniform mesh of 25×25 elements with three levels of refinement, $\eta_{upp} = 0.08$, $\eta_{low} = 0.01$ in adaptation criterion (18).

Fig. 13 shows the distribution of the non-zeros in the Jacobi matrix for Example 4.2 for both a uniform and an adapted mesh. In order to be able to plot the Jacobi matrix, we choose an uniform mesh of 20×20 square elements and the adapted mesh as an initially uniform mesh of 10×10 elements with one level of refinement. These two meshes have the same resolution in the interface region. From Fig. 13 we see that the Jacobi matrix of the adapted mesh contains less non-zeros than the one of the uniform mesh. This will be more obvious when a fine resolution is used in the interface region, and the adapted mesh contains far less elements than the uniform mesh as shown in Table 1.

It is noticeable that some new branches of non-zeros are present in the Jacobi matrix for the adapted mesh, which are caused by the local mesh refinement. We observe that in the Newton method, which is used to solve the non-linear algebraic equations resulting from the DIRK time integration method, the number of GMRES iterations for the adapted mesh (which is 2) is less than the number required for the uniform mesh (which is 4). Although the implementation of a DIRK method in combination with a locally refined mesh is non-trivial, we see from the examples discussed in this section that the DIRK method results in an efficient time integration method to solve the NSK equations on a locally refined mesh in combination with an LDG discretization.

4.3. Bubbles and droplets in contact with solid wall boundaries

In the next two numerical examples, we study a vapor bubble rising towards a solid wall and a liquid droplet on a solid substrate. It is pointed out that the shape of the vapor bubble and the liquid droplet depends on two factors [15]: (1) the
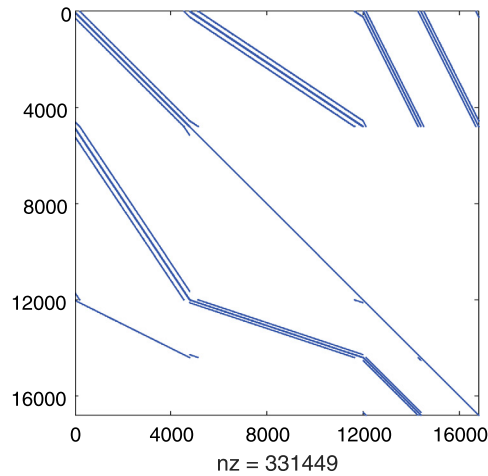
(a) a Jacobi matrix in a uniform mesh
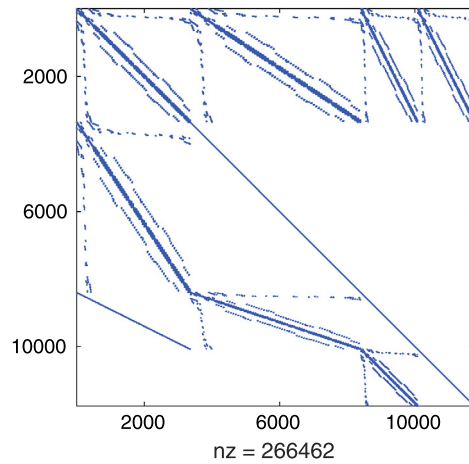
(b) a Jacobi matrix in an adapted mesh

Fig. 13. Shape of Jacobi matrix for Example 4.2 of the non-isothermal NSK equations on a uniform and an adapted mesh. Both meshes have the same resolution in the interface region. Initial conditions (22). Top matrix for a uniform mesh of 20×20 elements; Bottom: an initially uniform mesh of 10×10 elements with one level of refinement with $\eta_{upp} = 0.05$, $\eta_{low} = 0.01$ in (18).

contact angle and (2) the Bond number $\mathbb{B}o$. The contact angle is a parameter to model the physical interactions between the surface and the fluids, and is determined by whether the surface is hydrophilic or hydrophobic to the fluid. The contact angle has been studied theoretically [21] and numerically [13,12]. In the present simulation, the contact angle is imposed by the first equation in the boundary conditions (7) and ϕ is fixed to be $\pi/2$ for simplicity. The Bond number quantifies the relative importance of gravity against surface tension, and is defined as

$$\mathbb{B}o = \frac{\Delta \rho |\mathbf{g}| r^2}{\sigma}. \tag{23}$$

Here $\Delta \rho$ is the difference between the liquid and vapor mass density, $\mathbf{g}$ is the dimensionless gravity, r is the radius of the droplet or bubble and σ is the surface tension. The importance of the Bond number will be studied in the following numerical examples.

Example 4.3 (*Vapor bubble in contact with a solid wall*).

In this example, we will investigate the shape of a vapor bubble rising towards a solid wall, while accounting for the contact angle at the solid surface and the gravity. This example was studied in [13] for isothermal case by a model based on the second gradient theory on a uniform mesh. The parameters of the isothermal NSK equations are set to $\mathbb{R}e = 512$, $\mathbb{W}e = 65\,500$, the dimensionless temperature is set to $\theta = 0.85$.

The initial conditions are set as

$$\rho(\mathbf{x}, 0) = \frac{\rho_1 + \rho_2}{2} + \frac{\rho_2 - \rho_1}{2} \tanh\left(\frac{d(\mathbf{x}) - r}{2} \sqrt{\mathbb{W}e} \right),$$

(a) $t = 0$.   (b) $t = 0$.

(c) $t = 6$.   (d) $t = 6$.

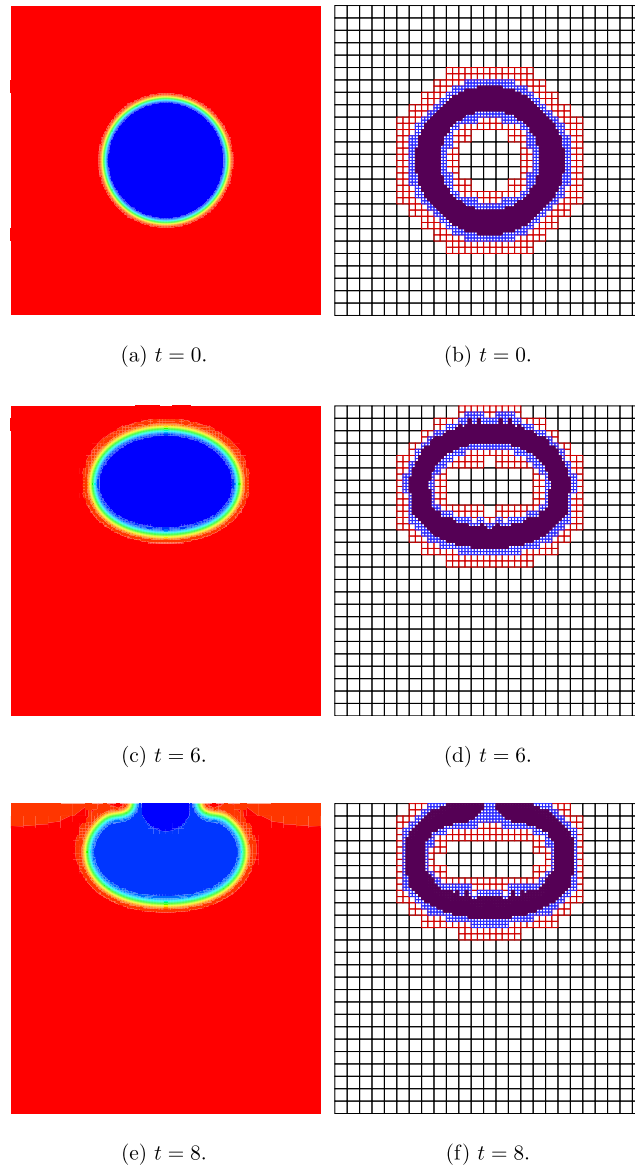(e) $t = 8$.   (f) $t = 8$.

Fig. 14. Example 4.3: time sequence and adapted mesh of a vapor bubble rising towards a solid wall, isothermal case. Initial conditions (24) and solid wall boundary conditions (7). Initially uniform mesh of 25×25 elements with three levels of refinement, $\eta_{upp} = 0.1$, $\eta_{low} = 0.02$ in adaptation criterion (18). $\mathbb{R}e = 500$, $\mathbb{W}e = 34\,455$, $|\mathbf{g}| = 0.02$. Left: density profile, Right: corresponding computational mesh.

$$\mathbf{u} = 0, \tag{24}$$

with $d(\mathbf{x}) = \sqrt{(x - 0.5)^2 + (y - 0.5)^2}$, $r = 0.2$ and $\rho_1 = 0.578$, $\rho_2 = 1.463$. The dimensionless gravity points in the negative y-direction with magnitudes $|\mathbf{g}| = 0.006, 0.02$. Because of relation (23), the Bond numbers are 0.18 and 0.6, respectively.

The time evolution of the bubble rising towards a wall under different values of gravity is presented in Figs. 14–17. From these figures, we see that

- the adaptive mesh follows the motion of the vapor bubble,
- the vapor bubble starts rising under the action of gravity, then attaches to the upper wall, and finally reaches an equilibrium state,
- the contact line moves rapidly after the contact of the bubble with the solid wall, as pointed out by [13],
- the gravity has an important impact on the shape of the bubble. Figs. 14–15 show that when the Bond number is large, the gravity makes the vapor bubble move to the upper solid wall and obtain a flattened shape in equilibrium. When the Bond number is relatively small, due to a smaller value of the gravitational acceleration, the bubble moves more slowly to the upper wall and obtains a spherical cap shape in equilibrium, as shown in Figs. 16–17.
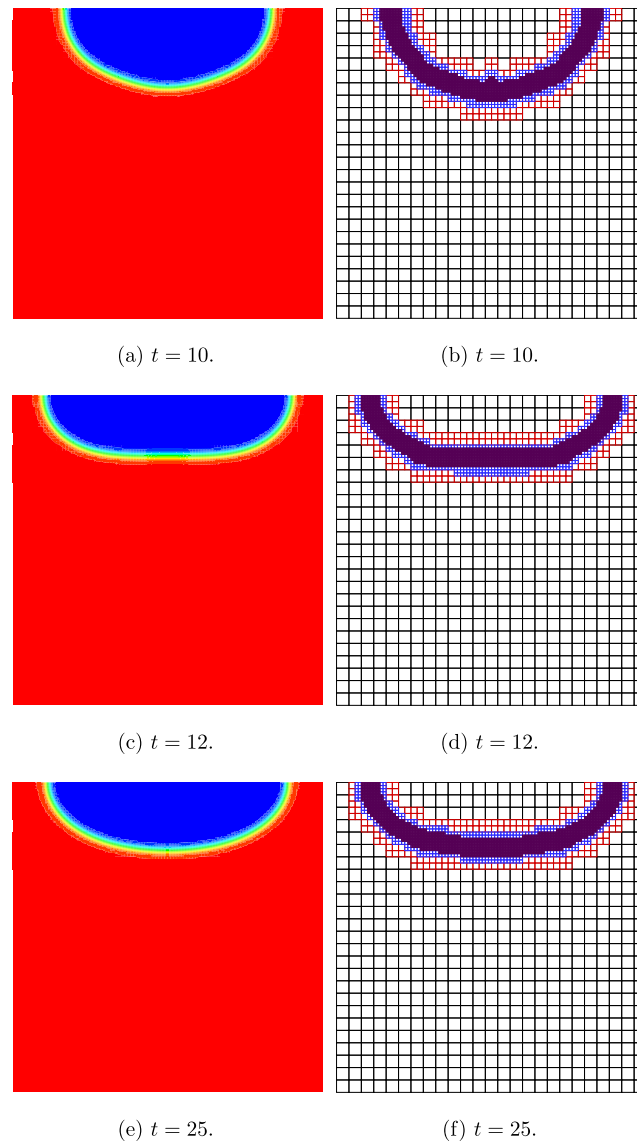
(a) $t = 10$.   (b) $t = 10$.

(c) $t = 12$.   (d) $t = 12$.

(e) $t = 25$.   (f) $t = 25$.

Fig. 15. Example 4.3: time sequence and adapted mesh of a vapor bubble rising towards a solid wall, isothermal case. Initial conditions (24) and solid wall boundary conditions (7). Initially uniform mesh of 25×25 elements with three levels of refinement, $\eta_{upp} = 0.1$, $\eta_{low} = 0.02$ in adaptation criterion (18). $\mathbb{R}e = 500$, $\mathbb{W}e = 34\,455$, $|\mathbf{g}| = 0.02$. Left: density profile, Right: corresponding computational mesh.

We also study the example of a bubble rising towards a wall for the non-isothermal case. Taking the parameters in the non-isothermal NSK equations as $Cv = 3.05$, $\mathbb{P}r = 0.13$, the results for the non-isothermal case are shown in Fig. 18. Given the same artificial gravity with $|\mathbf{g}| = 0.02$, the results for the non-isothermal case shown in Fig. 18, are similar to those for the isothermal case, shown in Figs. 14–15, except that the rising velocity and the wall attachment occurs slower.

Example 4.4 *(A liquid droplet on a solid wall).*

In this example the shape of a liquid droplet on a solid substrate, as used in wetting problems, is studied. This example was investigated using a (discontinuous) Galerkin method for the isothermal NSK equations in non-conservative form and on a uniform mesh [9,15]. The parameters of the isothermal NSK equations are set to $\mathbb{R}e = 512$, $\mathbb{W}e = 65\,500$, the dimensionless temperature is set to $\theta = 0.85$.

The initial conditions are set as

$$\rho(\mathbf{x}, 0) = \frac{\rho_1 + \rho_2}{2} - \frac{\rho_2 - \rho_1}{2} \tanh\left(\frac{d(\mathbf{x}) - r}{2} \sqrt{\mathbb{W}e}\right),$$
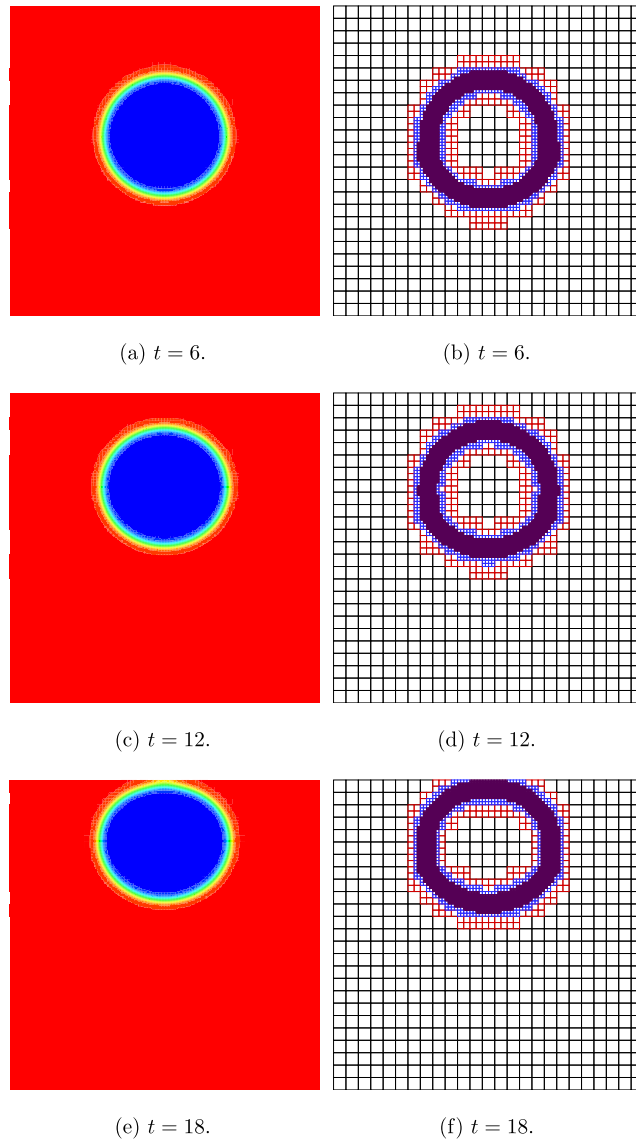
$$\mathbf{u} = 0, \tag{25}$$

Fig. 16. Example 4.3: time sequence and adapted mesh of a vapor bubble rising towards a solid wall, isothermal case. Initial conditions (24) and solid wall boundary conditions (7). Initially uniform mesh of 25 × 25 elements with three levels of refinement, $\mathbb{R}e = 500$, $\mathbb{W}e = 34\,455$, $|\mathbf{g}| = 0.006$. Left: density profile, Right: corresponding computational mesh.

with $d(\mathbf{x}) = \sqrt{(x - 0.5)^2 + y^2}$, $r = 0.2$ and $\rho_1 = 0.578$, $\rho_2 = 1.463$. At the initial time, a half spherical liquid droplet rests on a solid wall as shown in Fig. 19. The dimensionless gravity points in the negative y-direction with magnitude $|\mathbf{g}| = 0.008, 0.02, 0.05$. Recalling relation (23), the corresponding Bond numbers are 0.24, 0.60 and 1.49, respectively.

We perform the computations until time $t = 15.0$ and present the density profiles for different values of the dimensionless gravity in Fig. 20. Fig. 20 shows that the magnitude of the Bond number has an important effect on the shape of the droplet:

- when the Bond number is relatively small, the surface tension dominates and the droplet has the shape of a spherical cap in equilibrium,
- when the Bond number is relatively large, gravity, as the dominant force, flattens the droplet.

Table 1 shows the number of elements used in the adaptive mesh for Examples 4.3 and 4.4, which are much smaller than the number of elements required for a uniform mesh. Therefore, computing time and memory are saved when the adaptive LDG method is applied, compared to computations on a uniform mesh.
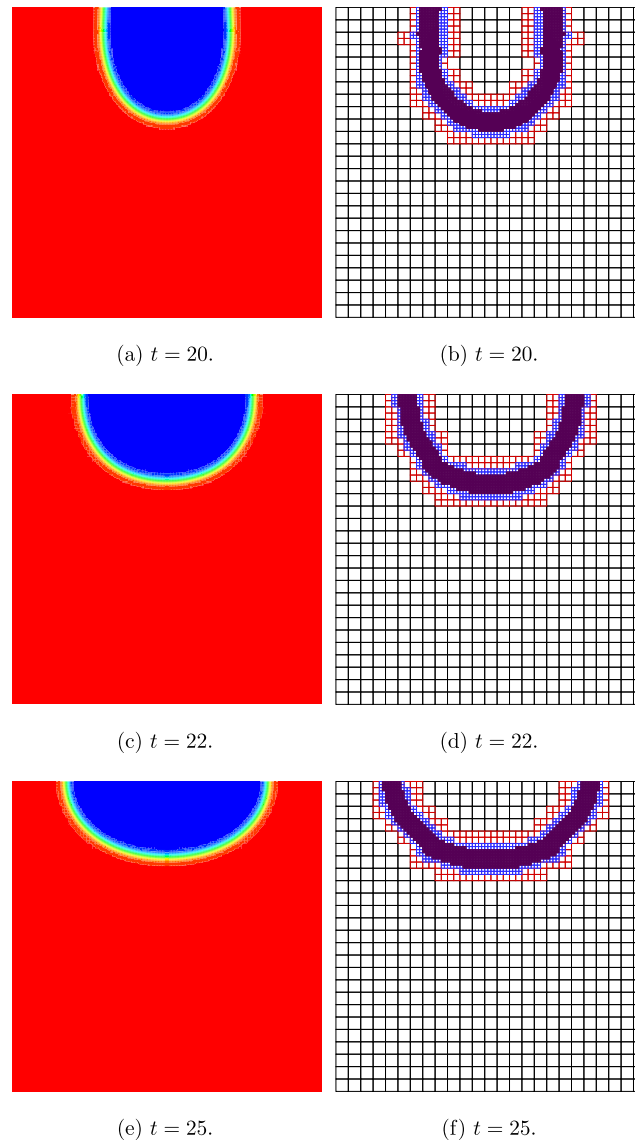
(a) $t = 20$.   (b) $t = 20$.

(c) $t = 22$.   (d) $t = 22$.

(e) $t = 25$.   (f) $t = 25$.

Fig. 17. Example 4.3: time sequence and adapted mesh of a vapor bubble rising towards a solid wall, isothermal case. Initial conditions (24) and solid wall boundary conditions (7). Initially uniform mesh of 25×25 elements with three levels of refinement, $\eta_{upp} = 0.1$, $\eta_{low} = 0.02$ in adaptation criterion (18). $\mathbb{R}e = 500$, $\mathbb{W}e = 34\,455$, $|\mathbf{g}| = 0.006$. Left: density profile, Right: corresponding computational mesh.

Remark 4.1. In the diffuse interface method using the Navier–Stokes–Korteweg equations, as discussed in this paper, the interface between two phases is automatically computed without the need of a separate interface reconstruction. The mathematical model, however, is practical only close to critical conditions, and requires a minimum number of elements in the interface. For more details, see [22].

5. Conclusions

In this article, an *h*-adaptive local discontinuous Galerkin method was presented for the (non)-isothermal NSK equations. In order to select candidate elements for refinement and coarsening, a criterion is provided to compute an indicator for the elements in the computational mesh based on the locally largest value of the density gradient. A strategy called "refinement must, coarsening can" is adopted in refining and coarsening the candidate cells. Numerical experiments demonstrate the accuracy, efficiency and capabilities of the local discontinuous Galerkin method for the (non)-isothermal NSK equations on an adapted mesh. In some of the simulations solid wall boundary conditions have been employed. We emphasize that only direct neighbors are used in the computation of the indicators for the elements in an adapted mesh, and the coarsening procedure is relatively simple. The implicit Runge–Kutta time integration method in combination with an adapted mesh is non-trivial, but results in an efficient time integration method for the NSK equations.
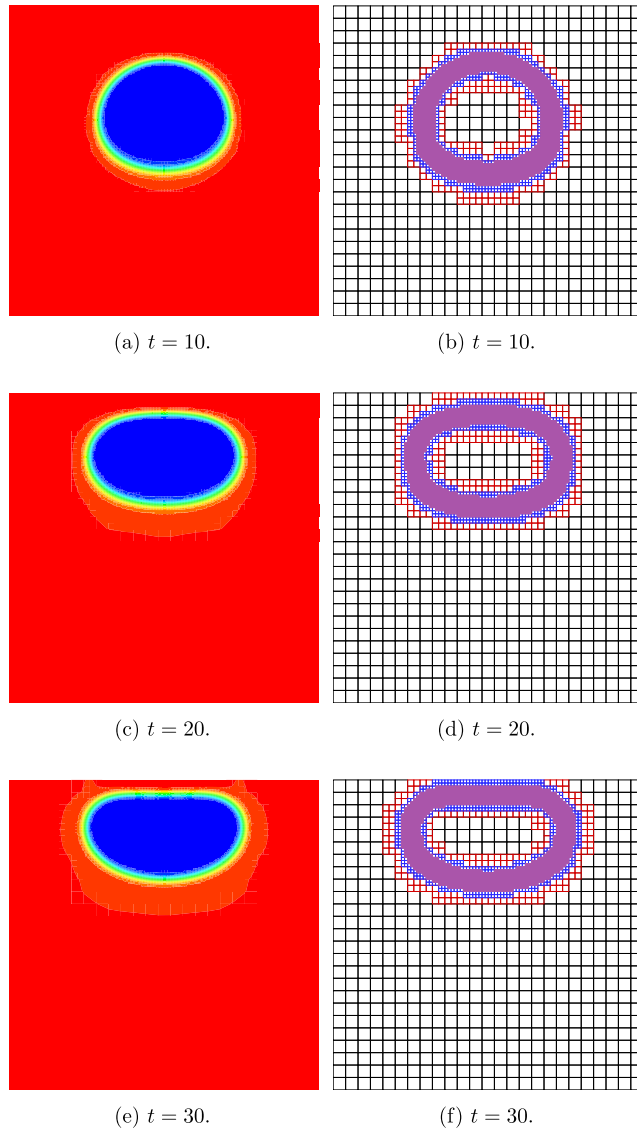
Fig. 18. Example 4.3: time sequence and adapted mesh of a vapor bubble rising towards a solid wall, non-isothermal case. Initial conditions (24) and solid wall boundary conditions (7). Initially uniform mesh of 25×25 elements with three levels of refinement, $\eta_{upp} = 0.1$, $\eta_{low} = 0.02$ in adaptation criterion (18). $\mathbb{R}e = 500$, $\mathbb{W}e = 34\,455$, $|\mathbf{g}| = 0.02$, $Cv = 3.05$, $\mathbb{P}r = 0.13$. Left: density profile, Right: corresponding computational mesh.
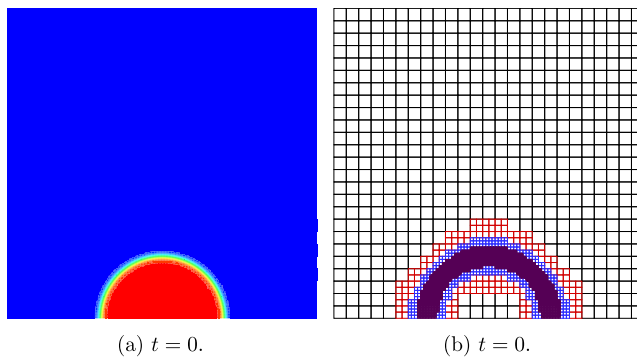

Fig. 19. Example 4.4: initial state of a droplet on a solid substrate with initial condition (25). Initially uniform mesh of 25×25 elements with three levels of refinement, $\eta_{upp} = 0.1$, $\eta_{low} = 0.02$ in adaptation criterion (18). Left: density profile, Right: corresponding computational mesh.
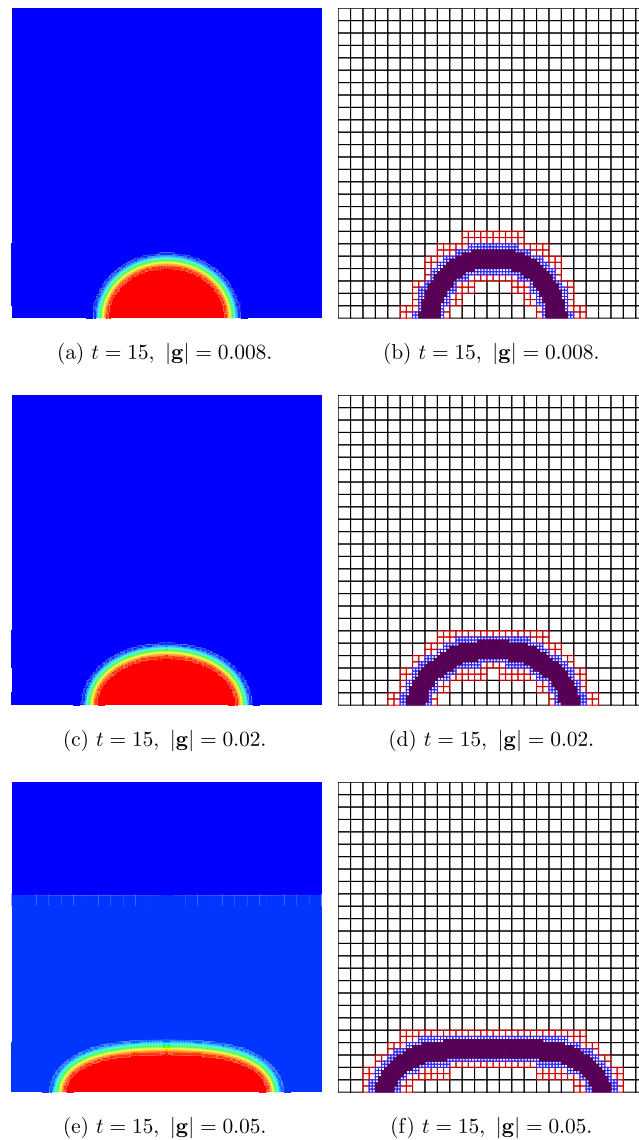
(a) $t = 15$, $|\mathbf{g}| = 0.008$.　　　　(b) $t = 15$, $|\mathbf{g}| = 0.008$.

(c) $t = 15$, $|\mathbf{g}| = 0.02$.　　　　(d) $t = 15$, $|\mathbf{g}| = 0.02$.

(e) $t = 15$, $|\mathbf{g}| = 0.05$.　　　　(f) $t = 15$, $|\mathbf{g}| = 0.05$.

Fig. 20. Example 4.4: a droplet on a solid substrate with initial condition (25) at the action of the dimensionless gravity with different magnitudes. Equilibrium state at $t = 15$, initially uniform mesh of 25×25 elements with three levels of refinement, $\eta_{upp} = 0.1$, $\eta_{low} = 0.02$ in adaptation criterion (18). $\mathbb{R}e = 500$, $\mathbb{W}e = 34455$. Left: density profile, Right: corresponding computational mesh.

Future research will investigate suitable criteria for mesh adaptation. Apart from the jump in the magnitude of the density, other indicators discussed in [19,28], a posteriori error estimates and residual analysis are also interesting options as criteria for refinement or coarsening. These latter approaches require, however, a significant theoretical effort.

Acknowledgements

References

[1] M. Ainsworth, J.T. Oden, A posteriori error estimation in finite element analysis, Comput. Methods Appl. Mech. Eng. 142 (1997) 1–88.
[2] R. Alexander, Diagonally implicit Runge–Kutta methods for stiff ODE's, SIAM J. Numer. Anal. 14 (1977) 1006–1021.

[3] M.J. Berger, P. Colella, Local adaptive mesh refinement for shock hydrodynamics, J. Comput. Phys. 82 (1989) 64–84.
[4] M. Braack, A. Prohl, Stable discretization of a diffuse interface model for liquid–vapor flows with surface tension, ESAIM Math. Model. Numer. Anal. 47 (2013) 401–420.
[5] J.W. Cahn, J.E. Hilliard, Free energy of a nonuniform system. I. Interfacial free energy, J. Chem. Phys. 28 (1958) 258–267.
[6] F. Coquel, D. Diehl, C. Merkle, C. Rohde, Sharp and diffuse interface methods for phase transition problems in liquid–vapour flows, IRMA Lect. Math. Theor. Phys. 7 (2005) 239–270.
[7] A. Dedner, C. Makridakis, M. Ohlberger, Error control for a class of Runge–Kutta discontinuous Galerkin methods for nonlinear conservation laws, SIAM J. Numer. Anal. 45 (2007) 514–538.
[8] J.L. Desmarais, J.G.M. Kuerten, Open boundary conditions for the Diffuse Interface Model in 1-D, J. Comput. Phys. 263 (2014) 393–418.
[9] D. Diehl, Higher order schemes for simulation of compressible liquid–vapor flows with phase change, PhD thesis, Universität Freiburg, 2007.
[10] D. Diehl, J. Kremser, D. Kröner, C. Rohde, Numerical solution of Navier–Stokes–Korteweg systems by local discontinuous Galerkin methods in multiple space dimensions, Appl. Math. Comput. 272 (2016) 309–335.
[11] J. Giesselmann, C. Makridakis, T. Pryer, Energy consistent discontinuous Galerkin methods for the Navier–Stokes–Korteweg system, Math. Comput. 83 (2014) 2071–2099.
[12] D. Jacqmin, Contact-line dynamics of a diffuse fluid interface, J. Fluid Mech. 402 (2000) 57–88.
[13] D. Jamet, O. Lebaigue, N. Coutris, J.M. Delhaye, The second gradient method for the direct numerical simulation of liquid–vapor flows with phase change, J. Comput. Phys. 169 (2001) 624–651.
[14] V. Jovanovic, C. Rohde, Error estimates for finite volume approximations of classical solutions for nonlinear systems of hyperbolic balance laws, SIAM J. Numer. Anal. 43 (2006) 2423–2449.
[15] J. Liu, H. Gomez, J.A. Evans, T.J. Hughes, C.M. Landis, Functional entropy variables: a new methodology for deriving thermodynamically consistent algorithms for complex fluids, with particular reference to the isothermal Navier–Stokes–Korteweg equations, J. Comput. Phys. 248 (2013) 47–86.
[16] J.T. Oden, W. Wu, M. Ainsworth, An a posteriori error estimate for finite element approximations of the Navier–Stokes equations, Comput. Methods Appl. Mech. Eng. 111 (1994) 185–202.
[17] M. Ohlberger, J. Vovelle, Error estimate for the approximation of nonlinear conservation laws on bounded domains by the finite volume method, Math. Comput. 75 (2006) 113–150.
[18] A. Pecenko, L.G.M. van Deurzen, J.G.M. Kuerten, C.W.M. van der Geld, Non-isothermal two-phase flow with a diffuse-interface model, Int. J. Multiph. Flow 37 (2011) 149–165.
[19] J. Qiu, C.W. Shu, A comparison of troubled-cell indicators for Runge–Kutta discontinuous Galerkin methods using weighted essentially nonoscillatory limiters, SIAM J. Sci. Comput. 27 (2005) 995–1013.
[20] C. Rohde, On local and non-local Navier–Stokes–Korteweg systems for liquid–vapour phase transitions, Z. Angew. Math. Mech. 85 (2005) 839–857.
[21] P. Seppecher, Moving contact lines in the Cahn–Hilliard theory, Int. J. Eng. Sci. 34 (1996) 977–992.
[22] L. Tian, Y. Xu, J.G.M. Kuerten, J.J.W. Van der Vegt, A local discontinuous Galerkin method for the (non)-isothermal Navier–Stokes–Korteweg equations, J. Comput. Phys. 295 (2015) 685–714.
[23] R. Verfürth, A posteriori error estimators for the Stokes equations, Numer. Math. 55 (1989) 309–325.
[24] R. Verfürth, A review of a posteriori error estimation techniques for elasticity problems, Comput. Methods Appl. Mech. Eng. 176 (1999) 419–440.
[25] R. Vilsmeier, D. Hänel, Adaptive methods on unstructured grids for Euler and Navier–Stokes equations, Comput. Fluids 22 (1993) 485–499.
[26] Y. Xu, C.W. Shu, Local discontinuous Galerkin methods for high-order time-dependent partial differential equations, Commun. Comput. Phys. 7 (2010) 1–46.
[27] H. Zhu, J. Qiu, Adaptive Runge–Kutta discontinuous Galerkin methods using different indicators: one-dimensional case, J. Comput. Phys. 228 (2009) 6957–6976.
[28] H. Zhu, J. Qiu, An *h*-adaptive RKDG method with troubled-cell indicator for two-dimensional hyperbolic conservation laws, Adv. Comput. Math. 39 (2013) 445–463.